

Article

# Large Eddy Simulation of Flow over Wavy Cylinders with Different Twisted Angles at a Subcritical Reynolds Number

Chunyu Guo , Hang Guo, Jian Hu \*, Kewei Song, Weipeng Zhang and Wei Wang

College of Shipbuilding Engineering, Harbin Engineering University, Harbin 150001, China

\* Correspondence: hujian791018@163.com

Received: 2 April 2019; Accepted: 10 July 2019; Published: 18 July 2019



**Abstract:** The deformation of the cylinder has been proved to greatly reduce the fluctuation of lift and the vortex-induced vibration. In this article, a new form of deformation mode for the smooth cylinder is proposed in order to reduce the vortex-induced vibrations, which can be applied to marine risers and submarine pipelines to ensure the working performance and safety of offshore platforms. Large eddy simulation (LES) is adopted to simulate the turbulent flow over wavy cylinders with three different twisted angles at a subcritical Reynolds number  $Re = 28,712$ . Comparing with the results of smooth cylinder, the maximum drag and lift reduction of wavy cylinder A3 with  $\alpha = 40^\circ$  can reach 17% and 84%, respectively, and the corresponding vortex formation length increases significantly, while the turbulence intensity decreases relatively. Meanwhile, the circumferential minimum pressure coefficient is greater than that of the smooth cylinder, which also provides a greater drag reduction for the cylinder. The surface separation line, turbulent kinetic energy distribution, and wake vortex structure indicate that the elongation of separated shear layer and wake shedding position is larger than that of the smooth cylinder, and the vorticity value in the near wake region decreases. A periodic vortex structure is generated along the spanwise direction, and a weaker and more stable Karman vortex street is reformed at a further downstream position, which ultimately leads to the reduction of drag and fluctuating lift of the wavy cylinder.

**Keywords:** large eddy simulation; drag reduction; lift fluctuation; vortex shedding; separated shear layer

## 1. Introduction

With the increase of water depth, the traditional fixed platforms can no longer meet the needs of this deep-sea marine engineering, and the floating structures are needed instead. No matter what floating scheme is adopted in the development of offshore oilfield, pipelines, and risers are the key components of marine infrastructures, and they are indispensable equipment for the exploitation of deep-water oil and gas. Regardless of the form of the risers, the reasonable design of them requires accurate estimation of the load suffered in the actual marine environment. Considering the fatigue damage caused by the dynamic response of the risers is an important part of riser design. Vortex-induced vibration [1] occurs in marine risers under the action of ocean currents. The motion of risers is an important factor for fatigue damage of structures. For marine platforms and risers, since they all have cylindrical shapes, the investigation of vortex-induced vibration over cylinders can have a significant effect on the fatigue damage and safety problems. In this regard, extensive researches have been performed on the issue. The main purpose of them is to study the mechanism of flow over a cylinder, so as to suppress the vortex-induced vibration of the cylinder. Because the properties of fluid are difficult to change, most of the studies focus on reducing the force and vortex-induced vibration of

the cylinder by varying the surface shape of the cylinder. Pastò [2], Zhao and Cheng [3], Wang et al. [4], Zhu et al. [5], Kang et al. [6], and Belloli et al. [7] studied the flow over a circular cylinder in laminar and turbulent states. It was found that even within different Reynolds number ranges as well as operating configurations, the phenomenon of vortex-induced vibrations would occur. Zou and Lin [8], Zhuang et al. [9], Xu and Ni [10], Lam et al. [11], Lam and Lin [12], and Jung and Yoon [13] also found that the lift and drag as well as the vortex-induced vibration of the wavy or twisted cylinders were reduced to varying degrees compared with the circular cylinders through numerical simulation and experiments. Therefore, it can be seen that the change in the surface shape of the cylinder can suppress the vortex-induced vibration. Since numerous investigations conducted by researchers mentioned above have proved that wavy or twisted cylinders can greatly reduce the amplitude of vortex-induced vibrations, by means of substituting wavy or twisted for smooth cylinders of marine risers and submarine pipelines will provide great help in suppressing the vortex-induced vibrations suffered from ocean currents, which ultimately bring tremendous benefit to oil and gas exploitation of offshore platforms. Unlike the deformation methods mentioned in the literature, we adopt another method of varying the shape of the cylinder, the purpose of which is to investigate the vibration reduction effect of this deformation mode on the cylinder.

Pastò [2] conducted wind tunnel experiments on the flow over a freely vibrating circular cylinder in laminar and turbulent states. The focus of the experiments was on the effects of the mass-damping parameter and the cylinder roughness. Moreover, Reynolds number also played a significant role on influencing the vibration. Even when a cessation of coherent vortex shedding in steady configuration within the critical Reynolds number range, a sharp drop in the drag force along with the vortex-induced vibrations of the cylinder were observed. Zhao and Cheng [3] numerically studied the vortex-induced vibration of a rigid cylinder with finite length in uniform steady flow. The results showed that the vortex shedding of a fixed cylinder was suppressed if the cylinder length was less than two times of the cylinder diameter. However, if the cylinder was allowed to vibrate, the vortex-induced vibration occurred at the cylinder length to diameter ratios of  $L/D = 1$  and  $2$ , and the response amplitudes of these two lengths were similar to that of a two-dimensional cylinder. The vortices shedding off from the two short cylinders were generated from the free end of the cylinder and were almost perpendicular to the span of the cylinder. Wang et al. [4] introduced a flow control method based on passive vortex generators (PVGs) to suppress vortex-induced vibration of circular cylindrical structures. A series of wind tunnel experiments were carried out and the results manifested that PVGs were effective. The maximum root-mean-square values of vibration amplitudes were suppressed by more than 80% by the following method: The PVGs with best parameters were attached to the cylinder surface. The pressure test results demonstrated that the appropriate design of PVGs was able to suppress the vortex shedding in the wake of the cylinder. Reducing the correlation of wake flow spanwise was helpful to control the amplitudes of vortex-induced vibration. Zhu et al. [5] numerically investigated two-degree-of-freedom vortex-induced vibrations of a circular cylinder with and without two smaller control cylinders. The influence of smaller control cylinders on the suppression of vortex-induced vibration was studied. Through a series of simulations, the motion trajectories, amplitude response, and temporal evolution of vortex shedding and streamlines were obtained. The results showed that small cylinders placed at  $45^\circ$  had a better suppression effect on downstream vector, but the effect varied at different Reynolds numbers. By injecting enough momentum into the boundary layer of the main cylinder and rotating control cylinders at a reasonable velocity, the vibration suppression effect was further improved. Kang et al. [6] proposed a new calculation method, the modified shear stress transport turbulence model, in order to accurately simulate the fluctuating lift and drag of a cylinder in vortex-induced vibration. The vortex-induced vibration of a two-degree-of-freedom cylinder was numerical simulated under three different initial conditions including uniform acceleration, uniform deceleration, and uniform velocity, respectively. By comparing and analyzing the vibration amplitude, frequency and fluid force, motion locus and vortex shedding, the results under uniform acceleration were more accurate. In addition, according to

the vortex shedding characteristics of uniform acceleration and deceleration, the hysteresis mechanism was able to be analyzed. Belloli et al. [7] created an experimental set-up in a large wind tunnel to study vortex-induced vibrations from circular cylinders at high Reynolds numbers. The mass ratio of the cylinder was 35, which was quite low compared with experiments in air due to its large dimensions but still much higher than that available in water. Coherent and highly organized vortex shedding produced by the post-critical flow regime were possible to achieve through increasing the surface roughness of the model. Simultaneous measurement of instantaneous fluid force calculated the integrated surface pressure distribution and model oscillation was realized by means of the experimental set-up. How to control vortex shedding to reduce fluid-induced vibration has become a challenging issue in the field of hydrodynamics. To solve these problems, multiple different methods including changing the shape and roughness of cylinder surface, and rotating the cylinder to reduce the fluctuation of lift and drag as well as the amplitude of vortex-induced vibration have been proposed by researchers. Zou and Lin [8] carried out the large eddy simulation of the flow around a sinusoidal wavy cylinder. The average drag coefficient of the wavy cylinder was smaller due to a longer wake vortex formation length than the corresponding circular cylinder. The fluctuating lift coefficient of the wavy cylinder was also greatly reduced. This wavy surface led to the formation of three-dimensional free shear layers which was more stable than the purely two-dimensional free shear layers. The free shear layers only existed in further downstream position and greatly changed the near wake structures and pressure distributions. Zhuang et al. [9] numerically simulated the three-dimensional unsteady flow around a rotating wavy cylinder. The results showed that the rotation speed of the wavy cylinder must be about two times of the straight rotating cylinder to obtain the same average lift. With the increase of cylinder rotation speed, the vortex formation length increased and the periodic shedding of the Karman vortex was suppressed. Through the visualization of three-dimensional vortex structures in the wavy cylinder wake at various rotation speeds, there existed an obvious difference in the vortex structures between a rotating wavy cylinder and a stationary wavy cylinder caused by the effect of surface rotation. Xu and Ni [10] numerically studied the supersonic flow over a wavy cylinder using the scale-adaptive simulation technology. The drag reduction and fluctuating lift suppression of the wavy cylinder in supersonic flow were not significant compared with subsonic flow. The results suggested that the wavy surface was ineffective for supersonic flow over a circular cylinder. This was due to the existence of bow shock wave and no large scale vortex shedding in the cylinder flow field. In addition, the quasi-steady flow state with converged wake behind the nodal position and the unsteady flow state with obvious vortex street behind the saddle position were discovered in the near wake of wavy cylinder. Lam et al. [11] investigated the near wake of a wavy cylinder using various experimental techniques in the  $Re$  range from 3000 to 9000. The results manifested that the average vortex formation length was more than half a wavelength of the wavy cylinder and longer than that of the circular cylinder, and vortex formation length also directly led to the reduction of drag and related fluctuating lift. The shear layers shed from the points near the saddle plane extended along the spanwise direction, while the shear layers near the nodal plane shrank and the separation speed increased simultaneously. The vortex streets of wavy cylinder wake were more irregular, and three-dimensional vortex structure became more fragile and interactive, and vortex streets in nodal plane were greater than that in saddle plane. Lam and Lin [12] carried out numerical simulations on various wavy cylinders with different wavelength ratios at  $Re = 3000$ . The results demonstrated that the near wake vortex structures of wavy cylinder exhibited a periodic variation due to the wavelike separation line along the spanwise direction. Although the vortex shedding frequency remained approximately unchanged, the free shear layer was more difficult to roll up and developed into a mature vortex structure at a further downstream position instead. For a wavy cylinder with spanwise waviness and wave amplitude, the drag reduction and suppression of lift fluctuation could be remarkable. Jung and Yoon [13] numerically simulated the flow characteristics of three different cylinders (smooth, wavy, and twisted) at  $Re = 3000$ . It was found that the drag and lift distribution of twisted cylinder decreased by 13% and 96% compared with that of smooth cylinder. Periodic transverse vorticity was generated along the spanwise direction.

The separation shear layers were seen to be relatively more stable and closer to the downstream, and the overall values of turbulent kinetic energy (TKE) distribution were also smaller than those of the smooth and wavy cylinder. Similar conclusions were obtained from the investigation of the effect of cross-sectional aspect ratio and Reynolds number. Zhou et al. [14] investigated a circular cylinder with smooth, grooved, and dimpled surface at Reynolds numbers ranging from  $7.4 \times 10^3$  to  $8 \times 10^4$  in an open channel and a towing tank. The results depicted that the mean drag and root mean square lift coefficients of cylinders with grooved and dimpled surface were smaller than those of smooth cylinder, and PIV results also showed that surface roughness of cylinders resulted in smaller recirculation region and vortex shedding strength than that of smooth cylinder. Wong et al. [15] carried out an experimental study on a cylinder vertically mounted and attached to a motor (providing constant rotation) in a free-surface water channel. The results indicated that the normalized frequency response of a rotating cylinder coincided with that of a free vibrating non-rotating cylinder. At the same reduced velocities as that of the superior branch of a non-rotating transversely oscillating cylinder, the maximum oscillation amplitude increased with non-dimensional rotation rate up to  $\alpha \approx 2$ . While  $\alpha$  is greater than 2, the amplitude began to decrease sharply, and the oscillation of cylinder desynchronized with the weakened and discontinuous vortex shedding. Jie and Liu [16] mainly researched the difference of force and vortex structure between a vibrissa-shaped cylinder and circular, elliptical, and wavy cylinders. The results demonstrated that fluctuation of lift force for vibrissa-shaped cylinder was 79.2% less than that of the circular cylinder, and only a relatively low crest was observed when the Strouhal number was 0.2. The vortex structure showed prominent three-dimensional characteristics, and the separation line in the recirculation zone revealed remarkable wavelike structure. Two symmetrical vortices were attached closely to the back side of the cylinder, leading to smaller fluctuations in velocity and wall pressure, which in turn helped to reduce the vortex-induced force and suppress its vibrations.

The Reynolds number range used in the calculation is subcritical Reynolds number, which is due to the complete turbulent wake after fluid separation on the cylinder surface [17]. Different from the methods mentioned in the literature above, the present study adopts the wavy mode of same diameter but different twisted angles, focusing on transforming the surface shape of cylinder to reduce the fluctuation of force and the vortex-induced vibration exerted on the cylinder. Large eddy simulation (LES) is capable of accurately and reasonably simulating complicated turbulence issues involving flow over a cylinder. In this study, three kinds of wavy cylinders as well as a smooth cylinder are numerically simulated using three-dimensional LES. Through the analysis of drag and lift fluctuation coefficient, Strouhal number, velocity distribution and vortex formation length, pressure distribution and 3D separation, turbulent kinetic energy and wake vortex structure, the effects of twisted and rotation angle of wavy cylinders in subcritical Reynolds number range on the above parameters are investigated systematically.

## 2. Mathematical Model

### 2.1. Governing Equations

A three-dimensional large eddy simulation turbulence model [18] is employed to numerically simulate the flow over various cylinders in the present study. The basic idea of LES is to solve larger scale eddies directly and to simulate smaller scale eddies by a subgrid-scale stress turbulence (SGS) model. Instead of time-averaging, LES uses a spatial filtering operation to separate the larger and smaller eddies. Therefore, the Navier-Stokes and continuum equations of the filtered incompressible flow are the LES governing equations:

$$\frac{\partial \bar{u}_i}{\partial t} + \frac{\partial \bar{u}_i \bar{u}_j}{\partial x_j} = -\frac{1}{\rho} \frac{\partial \bar{p}}{\partial x_i} + \nu \frac{\partial^2 \bar{u}_i}{\partial x_j \partial x_j} - \frac{\partial \tau_{ij}}{\partial x_j}, \tag{1}$$

$$\frac{\partial \bar{u}_i}{\partial x_i} = 0, \tag{2}$$

where  $\bar{u}_i$  are the filtered velocity components along the Cartesian coordinates  $x_i$ ,  $t$  is the time,  $\bar{p}$  is the pressure,  $\rho$  is the fluid density, and  $\nu$  is the kinematic viscosity of the fluid, and the overbar denotes the large (or resolved) scale obtained from grid filtering. Subgrid-scale stress tensor ( $\tau_{ij}$ ) is defined as  $\tau_{ij} = \overline{u_i u_j} - \bar{u}_i \bar{u}_j$ , similar to Reynolds stress, subgrid-scale stress filters out momentum transport between small-scale pulsation and resolved-scale turbulence. In order to realize large eddy numerical simulation, a sealing model of subgrid-scale stress must be constructed. Subgrid-scale stress turbulence model is the key to implement large eddy numerical simulation successfully.

Under normal circumstances the subgrid-scale model is based on eddy viscosity model, which is on the basis of the artificial eddy viscosity method, and the influence of turbulence is concentrated on the turbulent viscosity. In this method, subgrid-scale kinetic energy dissipation is considered to be similar to molecular diffusion. Consequently, the expression of  $\tau_{ij}$  is as follows:

$$\tau_{ij} - \frac{1}{3} \tau_{kk} \delta_{ij} = -2\nu_t \bar{S}_{ij}, \tag{3}$$

where  $\nu_t$  is the turbulent eddy viscosity coefficient and  $\bar{S}_{ij}$  is the strain rate tensor for the resolved scale defined by

$$\bar{S}_{ij} = \frac{1}{2} \left( \frac{\partial \bar{u}_i}{\partial x_j} + \frac{\partial \bar{u}_j}{\partial x_i} \right). \tag{4}$$

The subgrid-scale eddy viscosity model adopted in this study is the WALE (Wall-Adapting Local-Eddy Viscosity) model [19], which is a more modern subgrid scale model that uses a novel form of the velocity gradient tensor in its formulation. The WALE subgrid scale model provides the following mixing-length type formula for the subgrid scale viscosity:

$$\nu_t = \rho \Delta^2 S_w \tag{5}$$

where  $\rho$  is the fluid density,  $\Delta$  is the length scale or grid filter width [20], and  $S_w$  is a deformation parameter. The length scale  $\Delta$  is defined in terms of the cell volume  $V$  as:

$$\Delta = \begin{cases} C_w V^{1/3} & \text{if length scale limit is not applied} \\ \min(\kappa d, C_w V^{1/3}) & \text{if length scale limit is applied} \end{cases}, \tag{6}$$

where  $C_w$  is a model coefficient,  $\kappa$  is the von Karman constant, and the value of  $\kappa$  is 0.41. The deformation parameter  $S_w$  is defined as:

$$S_w = \frac{\left( S_{ij}^d S_{ij}^d \right)^{3/2}}{\left( \bar{S}_{ij} \bar{S}_{ij} \right)^{5/2} + \left( S_{ij}^d S_{ij}^d \right)^{5/4}}, \tag{7}$$

where the tensor  $S_{ij}^d$  is defined as:

$$S_{ij}^d = \frac{1}{2} (\bar{g}_{ij}^2 + \bar{g}_{ji}^2) - \frac{1}{3} \delta_{ij} \bar{g}_{kk}^2, \quad \bar{g}_{ij} = \frac{\partial \bar{u}_i}{\partial x_j}. \tag{8}$$

The model coefficient  $C_w$  is not universal. Typical values of  $C_w$  reported in the literature range from 0.5, for homogeneous isotropic decaying turbulence, to 0.325, for channel flows. In the present study the default value of  $C_w = 0.544$  [19] were validated using STAR-CCM+ [21] to prove that it works well for both homogeneous, isotropic decaying turbulence and for channel flows.

## 2.2. Numerical Method

Three-dimensional, incompressible, separated flow, constant density, and unsteady simulation were performed in this study. The Navier-Stokes equation was solved by applying the finite volume

method (FVM) on unstructured grids. In LES simulation, the SIMPLE algorithm was adopted to solve the pressure-velocity coupling equation. A bounded central difference discretization scheme [22] was used for spatial discretization while a second-order implicit scheme was employed to advance the equations in time, and the Hybrid Gauss-LSQ method was used to deal with gradient computation.

### 3. Numerical Setting

#### 3.1. Computational Model

Four different kinds of cylinders are selected for numerical simulation, including a smooth cylinder and wavy cylinders with three different twisted angles. The diameter and spanwise length of the four cylinders are uniform, corresponding to  $D$  and  $6D$ , respectively. The wavy cylinder is composed of three identical cylinders with a wavelength of  $\lambda = 2D$ . The shape of wavy cylinder is defined by the twisted angle  $\alpha$ , which is the angle at which the cross section along spanwise of the cylinder rotates around a point  $O$  on the circumference. It is stipulated that the rotation along the counter-clockwise direction is positive, and  $\alpha$  has the following relationship with the spanwise coordinate  $z$  of the section:

$$\alpha = \alpha_{\max} \sin\left(\frac{\pi z}{D}\right), \tag{9}$$

where  $\alpha_{\max}$  is the maximum twisted angle, as shown in Figure 1. In the previous calculation, it was found that the force coefficients and flow field distribution of the wavy cylinders were approximately the same as that of the smooth cylinder when  $\alpha_{\max} < 20^\circ$ , as a result, the simulation is implemented under the condition of  $\alpha_{\max} > 20^\circ$ . The maximum twisted angles of wavy cylinder A1, A2, and A3 correspond to  $20^\circ$ ,  $30^\circ$ , and  $40^\circ$ , respectively.

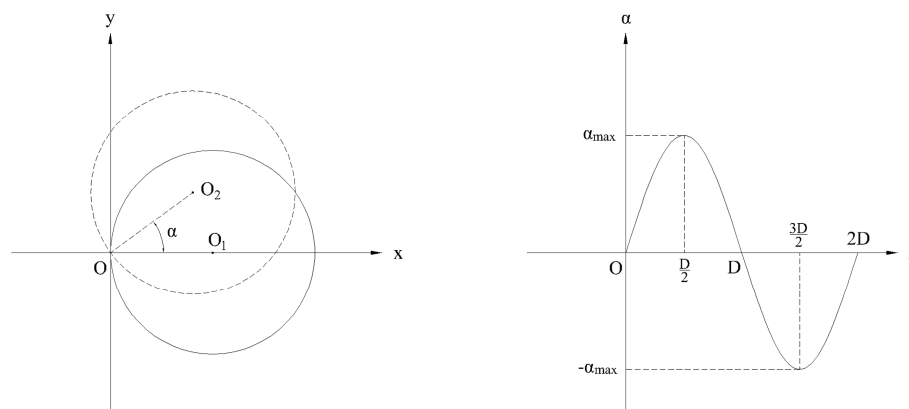


**Figure 1.** Definition of twisted angle and its variation relationship with the spanwise coordinate.

On account of that wavy cylinder does not have the geometric symmetry of smooth cylinder, it is imperative to conduct simulations on wavy cylinders with different rotation angles. Rotation angle  $\theta$  is defined as the rotation angle of the cylinder around its central axis, and eight rotation angles are selected in this study, which correspond to  $\theta = 0^\circ, 45^\circ, 90^\circ, 135^\circ, 180^\circ, 225^\circ, 270^\circ,$  and  $315^\circ$ , respectively. In order to better analyze the flow characteristics over a cylinder, three sections, A, B, and C, are chosen in spanwise direction, and the corresponding spanwise coordinates  $z$  are  $2.5D, 3D,$  and  $3.5D$ , respectively. The corresponding nodal and saddle plane are shown in Figure 2.

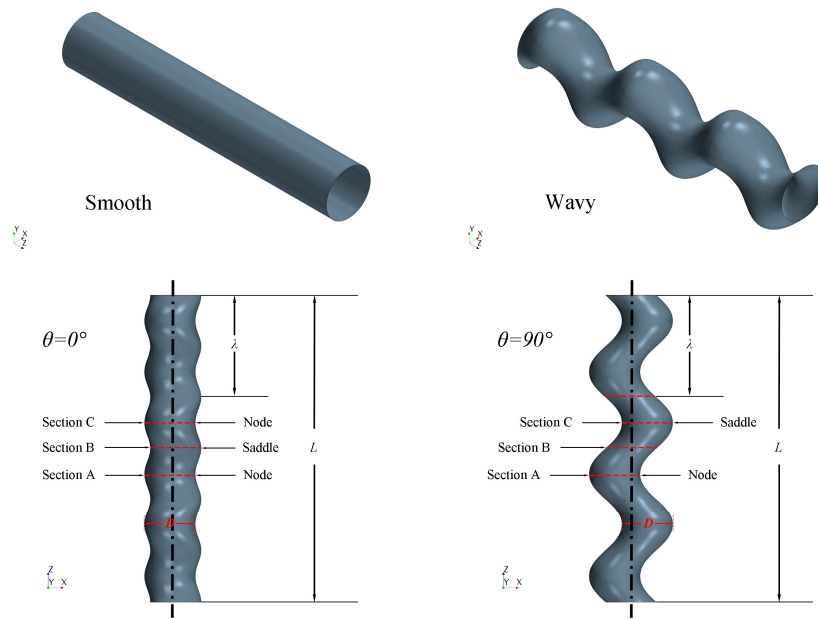


Figure 2. Smooth, wavy cylinder and its geometric definition.

### 3.2. Computational Domain and Boundary Conditions

The computational domain and boundary conditions are shown in Figure 3. The dimension of the computational domain is set at  $24D \times 16D \times 6D$  in the  $x, y, z$  directions of a fixed Cartesian coordinate system ( $x, y, z$ ). The origin of the coordinate system is located at the end of the cylinder. The direction of the  $x$ -axis is aligned with the inlet flow direction (streamwise direction), the direction of the  $z$ -axis is parallel to the cylinder center axis (spanwise direction), and the  $y$ -axis is perpendicular to the  $x$ -axis and the  $z$ -axis (crosswise direction). The distance between the upstream boundary and the origin in the streamwise direction is  $8D$ , and the downstream boundary is  $16D$  away from the origin. The distance between the origin and the upper and lower boundaries in the crosswise direction are both  $8D$ . The spanwise length is identical to that of the cylinder. The Reynolds number based on the diameter  $D$  of cylinder and freestream velocity  $U_\infty$  is  $Re = U_\infty D / \nu = 28712$  in the present simulations. The boundary conditions of the computational domain are set as follows: The inlet boundary is set to the velocity inlet, and the outlet boundary is set as the pressure outlet. The other four boundaries are set to symmetry plane by considering an infinitely long cylindrical structure, while the cylinder is set to the no-slip wall.

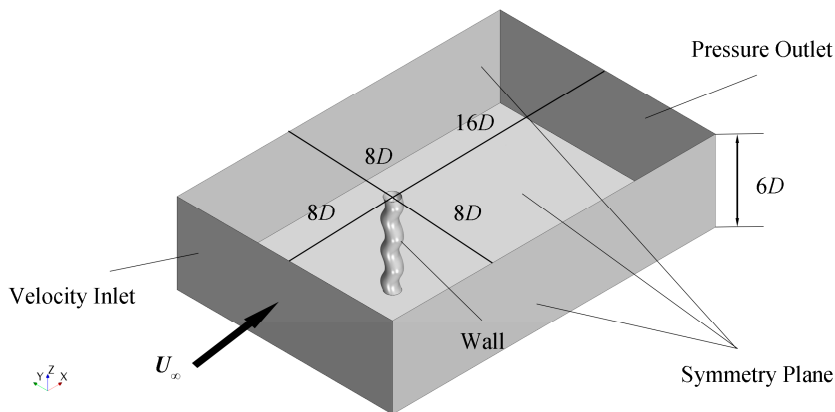
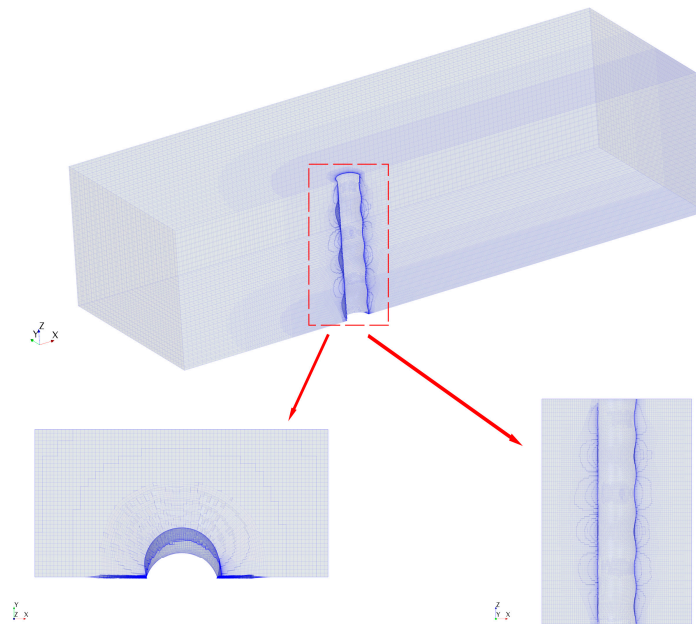


Figure 3. Schematic of the computational domain and boundary conditions.

Unstructured mesh is adopted for mesh discretization in the computational domain. Figure 4 depicts the volume mesh in the computational domain and near the boundary layer of wavy cylinder.

In order to meet the computing requirements of large eddy simulation, the distance from the cylinder surface to the nearest mesh points are fixed at  $y^+$  less than 1. In order to better capture the vortex structure in the wake region of the cylinder, the mesh in the downstream direction is refined, and the size of the mesh in the boundary layer gradually increases to the refined region at an appropriate ratio. The dimensionless time step employed in the computation is defined as  $T = U_\infty \Delta t / D$ . For all current simulations, at least 500 dimensionless time steps were taken, corresponding to about 100 cycles of vortex shedding to obtain more reliable statistical information, which were larger than the time steps and shedding cycles calculated in Lam and Lin [12].



**Figure 4.** Mesh distributions in computational domain and near boundary layer of wavy cylinder.

#### 4. Numerical Model Validation

##### 4.1. Validation for Smooth Cylinder

As the accuracy of LES calculation depends on the number of mesh elements and time step, it is essential to perform a grid and time-step independence verification on the smooth cylinder and the wavy cylinders. To quantitatively verify the numerical calculation method and the accuracy of the grid, the time average drag coefficient ( $\overline{C_D}$ ), the lift coefficient fluctuation root mean square (r.m.s.) value ( $C_{L,rms}$ ), and the Strouhal number ( $St$ ) of the smooth cylinder are compared with the experimental values. The drag coefficient ( $C_D$ ) and lift coefficient ( $C_L$ ) are defined as follows:

$$C_D = \frac{2F_D}{\rho U_\infty^2 DL}, \tag{10}$$

$$C_L = \frac{2F_L}{\rho U_\infty^2 DL}, \tag{11}$$

where  $\rho$  is the fluid density,  $U_\infty$  is the inflow velocity,  $D$  is the diameter of the cylindrical section,  $L$  is the spanwise length of the cylinder, and  $F_D$  and  $F_L$  are the total drag and lift, respectively. The total force is the sum of friction and pressure force calculations, and  $F_D$  and  $F_L$  are the total force of the cylinder in the streamwise and crosswise direction, respectively. The Strouhal number is a dimensionless vortex shedding frequency ( $f_s$ ), expressed as

$$St = \frac{f_s D}{U_\infty} \tag{12}$$

The vortex shedding frequency,  $f_s$ , is obtained from the fast Fourier transform (FFT) of the time–history curve of the lift coefficient.

First, grid-independent verification is performed on the smooth cylinder. Table 1 shows three sets of grids of different numbers.  $S_i$  ( $i = 1, 2, 3$ ) represents the calculation results corresponding to the coarse, medium, and fine grids. Following Baek et al.’s [23] similar approach of treating unstructured meshes, the refinement ratio is an important parameter that needs to be determined before grid-independent verification. The refinement ratio  $r_G$  is defined as follows:

$$r_G = \left( \frac{N_{fine}}{N_{coarse}} \right)^{1/d} \tag{13}$$

**Table 1.** Grid independence verification on smooth cylinder.

Smooth Cylinder	$T$	Grid	$\bar{C}_D$	Error (%)	$C_{L,rms}$	Error (%)	$St$	Error (%)
EFD	-	-	1.1356		0.2995		0.2046	
coarse ( $S_1$ )	0.02	2.42M	1.0325	9.08	0.3206	7.05	0.2105	2.88
medium ( $S_2$ )	0.02	4.18M	1.0781	5.06	0.2925	2.34	0.209	2.15
fine ( $S_3$ )	0.02	7.22M	1.1151	1.81	0.3073	2.60	0.2087	2.00

Here,  $N$  is the total number of mesh elements and  $d$  is the number of dimensions. As the simulations in this study are three-dimensional,  $d$  is set as 3. The refinement ratio of the three sets of grids is about 1.2, and the dimensionless time step is taken as  $T = 0.02$ . Table 1 presents the calculation results of grid-independent verification on the smooth cylinder when  $Re = 28,712$ , which illustrates the comparison between the calculation results and the experimental values [24]. EFD in Table 1 is the abbreviation of Experimental Fluid Dynamics, which corresponds to the experimental values of the smooth cylinder. According to the relative errors mentioned in Jie and Liu [16], a reasonably good agreement between the simulation and experiment data was reached under the condition that the errors were less than 8.5%. Table 1 shows that the errors of  $\bar{C}_D$ ,  $C_{L,rms}$ , and  $St$  gathered from the LES method except the coarse grid ( $S_1$ ) can meet the condition of less than 8.5%, which indicates a good consistency with the experimental values.

Second, the time–step independence verification on the smooth cylinder is conducted. Table 2 shows three dimensionless time steps, where  $S_i$  ( $i = 4, 5, 6$ ) represents the calculation results with small, medium, and large time steps. In this paper, medium mesh with 4.18 million elements is adopted for all three time steps. It can be found that only  $S_6$  has a large discrepancy compared with the experiment results, and the errors of  $S_4$  and  $S_5$  were all under 8.5%, showing a reasonably good agreement with the experiment data. Therefore, while ensuring the accuracy and efficiency of the calculation, the medium mesh contained 4.18 million elements accompanied with the dimensionless time step of  $T = 0.02$  were ultimately selected in this study.

**Table 2.** Time–step independence verification on smooth cylinder.

Smooth Cylinder	$T$	Grid	$\bar{C}_D$	Error (%)	$C_{L,rms}$	Error (%)	$St$	Error (%)
EFD	-	-	1.1356		0.2995		0.2046	
small ( $S_4$ )	0.01	4.18M	1.1081	2.42	0.3063	2.27	0.2089	2.10
medium ( $S_5$ )	0.02	4.18M	1.0781	5.06	0.2925	2.34	0.209	2.15
large ( $S_6$ )	0.04	4.18M	0.9007	20.69	0.1729	42.27	0.2137	4.45

#### 4.2. Validation for Wavy Cylinder

The grid and time–step independence verifications were also performed on the wavy cylinders. The wavy cylinder A1 ( $\theta = 0^\circ$ ) with  $\alpha = 20^\circ$  was selected for the calculation. The results are shown in Tables 3 and 4, respectively. For a better comparison with the smooth cylinder, the number of meshes and the time steps of the wavy and smooth cylinders were kept the same. The following tables show

that the number of grid elements and the time steps had little influence on the calculation results of  $\bar{C}_D$ ,  $C_{L,rms}$ , and  $St$ , and thus, it can be concluded that the results of the grid and time-step independence verification on the wavy cylinder are satisfactory. Finally, the medium mesh with 4.18 million elements was selected with the dimensionless time step of  $T = 0.02$ .

**Table 3.** Grid independence verification on wavy cylinder.

Wavy Cylinder	$T$	Grid	$\bar{C}_D$	$C_{L,rms}$	$St$
coarse ( $W_1$ )	0.02	2.42M	1.0728	0.2758	0.2075
medium ( $W_2$ )	0.02	4.18M	1.1125	0.3003	0.2115
fine ( $W_3$ )	0.02	7.22M	1.1359	0.3213	0.2125

**Table 4.** Time-step independence verification on wavy cylinder.

Wavy Cylinder	$T$	Grid	$\bar{C}_D$	$C_{L,rms}$	$St$
small ( $W_4$ )	0.01	4.18M	1.1149	0.3101	0.2114
medium ( $W_5$ )	0.02	4.18M	1.1125	0.3003	0.2115
large ( $W_6$ )	0.04	4.18M	1.1191	0.3149	0.2127

## 5. Results and Analysis

### 5.1. Force and Strouhal Number

To save the computational resources and time required for large eddy simulation, the similarity between different rotation angles of the wavy cylinder was verified. Taking the wavy cylinder A1 with  $\alpha = 20^\circ$  as an example, eight rotation angles ( $\theta = 0^\circ, 45^\circ, 90^\circ, 135^\circ, 180^\circ, 225^\circ, 270^\circ, \text{ and } 315^\circ$ ) were selected for calculation. The calculation results in Table 5 show that the force coefficients and Strouhal numbers of  $0^\circ$  and  $180^\circ$ ,  $45^\circ$  and  $225^\circ$ ,  $90^\circ$  and  $270^\circ$ ,  $135^\circ$  and  $315^\circ$  were basically identical, respectively. However, those of the four groups of angle differ from each other. Thus, it can be preliminarily concluded that there is a partial similarity between different angles of the wavy cylinder. This conclusion will be further validated in Sections 5.2 and 5.3.

**Table 5.** Force coefficients and Strouhal numbers of different rotation angles of wavy cylinder A1.

$\theta$	$\bar{C}_D$	$C_{L,rms}$	$St$
0	1.1125	0.3003	0.2115
45	0.943	0.0877	0.209
90	0.8956	0.0489	0.1962
135	0.9232	0.0692	0.2103
180	1.0735	0.2671	0.211
225	0.9318	0.0844	0.2064
270	0.8864	0.0463	0.1911
315	0.9271	0.0659	0.2102

Due to the partial similarity of the wavy cylinder, only four rotation angles ( $\theta = 0^\circ, 45^\circ, 90^\circ, 135^\circ$ ) were selected for the calculation. Figure 5 shows the force coefficients and Strouhal numbers of the smooth cylinder and three wavy cylinders with  $Re = 28,712$ . According to Figure 5a, besides  $\theta = 0^\circ$ , the average drag coefficients  $\bar{C}_D$  of the three wavy cylinders with other three rotation angles are reduced by approximately 12% to 19%, compared to the smooth cylinder. However, when  $\theta = 0^\circ$ , the  $\bar{C}_D$  of the wavy cylinder A1 becomes larger than the smooth cylinder, and A2 is reduced by less than 2%, while A3 is reduced by 11%. Similar to Figure 5a, Figure 5b shows that when  $\theta$  is not  $0^\circ$ , the r.m.s. values of lift fluctuation  $C_{L,rms}$  of the three wavy cylinders with other three rotation angles are reduced by 60% to 87% compared to the smooth cylinder. However, when  $\theta = 0^\circ$ , the  $C_{L,rms}$  of the wavy cylinder A1 becomes slightly larger than the smooth cylinder, and A2 is reduced by about

26%, while A3 is reduced by 68%. According to Figure 5a,b, only the wavy cylinder A3 has a relatively large reduction in the lift and drag coefficients compared to the smooth cylinder. The drag and lift coefficients of the other two wavy cylinders decrease slightly, or even increase, when  $\theta = 0^\circ$ . Figure 5c shows that the Strouhal numbers of all three wavy cylinders are all in the vicinity of 0.2, similarly to the smooth cylinder. The Strouhal number of the smooth cylinder in the subcritical Reynolds number range, according to Sumer and Fredsøe [24], was around 0.2. Therefore, it can be concluded that the variation of the Reynolds number or the geometry of the cylindrical surface had little influence on the shedding frequency of the wake vortex.

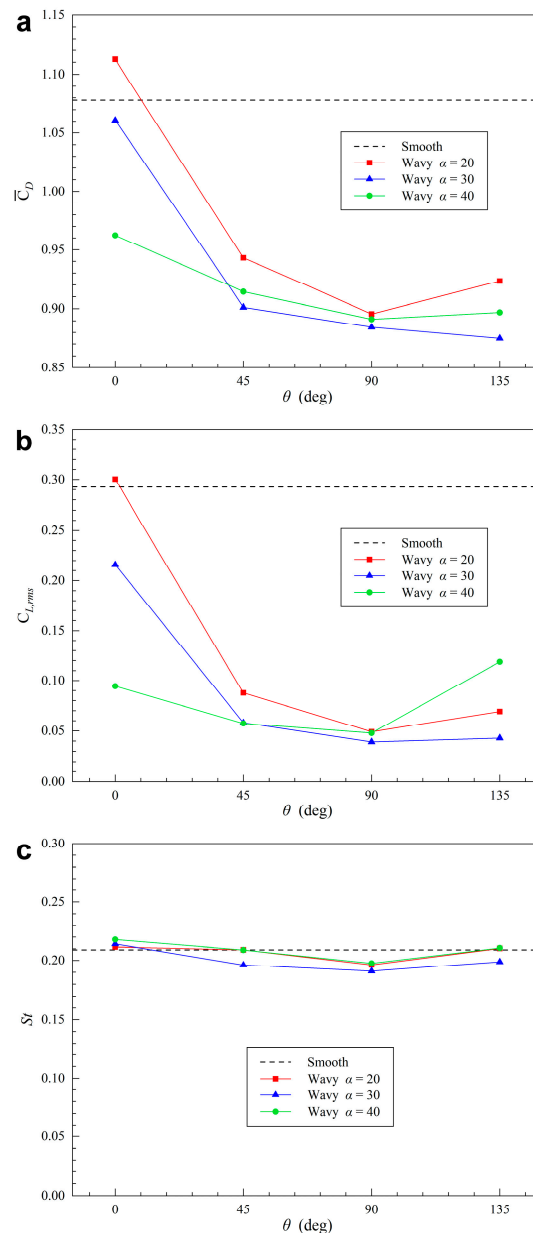


**Figure 5.** Comparison of (a) average drag coefficients, (b) r.m.s. values of lift fluctuation, and (c) Strouhal numbers of three wavy cylinders and the smooth cylinder.

### 5.2. Velocity Distribution and Vortex Formation Length

The cylinder wake vortex formation length is very important because it has an impact on the cylinder wake pressure and force coefficient. The definition of the wake vortex length is not universal, and different researchers have proposed different methods [25–29]. The locations of the time-averaged

closure point ( $P_{U0}$ ) when the normalized average streamwise velocity is zero and the point of the maximum normalized r.m.s. value of streamwise velocity fluctuation ( $P_{U_{rms}}$ ) on the wake centerline ( $y = 0$  plane) are often adopted to define the vortex formation length. Therefore, the wake vortex formation length includes the wake closing length  $L_{fc}$  when the average streamwise velocity is zero ( $U/U_\infty = 0$ ) and the maximum turbulence intensity length  $L_{fti}$  when the r.m.s. value of streamwise velocity fluctuation ( $u'/U_\infty$ ) reaches a maximum.

First, the partial similarity of the wavy cylinder A1 was further verified. Figure 6 depicts the normalized average streamwise velocity of the wavy cylinder A1 with  $\alpha = 20^\circ$  along the wake centerline ( $y = 0$  plane), showing the velocity at the three sections in the spanwise direction of the cylinder at eight rotation angles ( $\theta$  ranging from  $0^\circ$  to  $315^\circ$ ). A comparison of Figure 6a,c demonstrates that the average streamwise velocity at  $\theta = 0^\circ$  at sections A, B, and C is basically the same as that at  $\theta = 180^\circ$  at sections C, B, and A, respectively. This is due to, after the rotation, section A of  $\theta = 0^\circ$  and section C of  $\theta = 180^\circ$  are the sections with the same coordinate position, and section B is a circle centered at the origin of the coordinate, hence the coordinate position remains unchanged. Therefore, it is believed that  $\theta = 0^\circ$  and  $\theta = 180^\circ$  share similarity, which is consistent with the conclusion in 5.1. It can also be found that  $\theta = 45^\circ$  and  $\theta = 225^\circ$ , as well as  $\theta = 90^\circ$  and  $\theta = 270^\circ$ , and  $\theta = 135^\circ$  and  $\theta = 315^\circ$  in Figure 6b are likewise similar, indicating that the partial similarity of the wavy cylinder concluded in 5.1 is valid. In addition, it can be found that only when  $\theta = 0^\circ$  and  $\theta = 180^\circ$ , the zero points of average streamwise velocity are almost the same as those of the smooth cylinder, while the zero points of other angles are located at further downstream positions of the cylinder wake. This indicates that besides  $\theta = 0^\circ$  and  $\theta = 180^\circ$ , other angles have a great impact on the control of the cylindrical wake vortex structure and the lift and drag reduction.

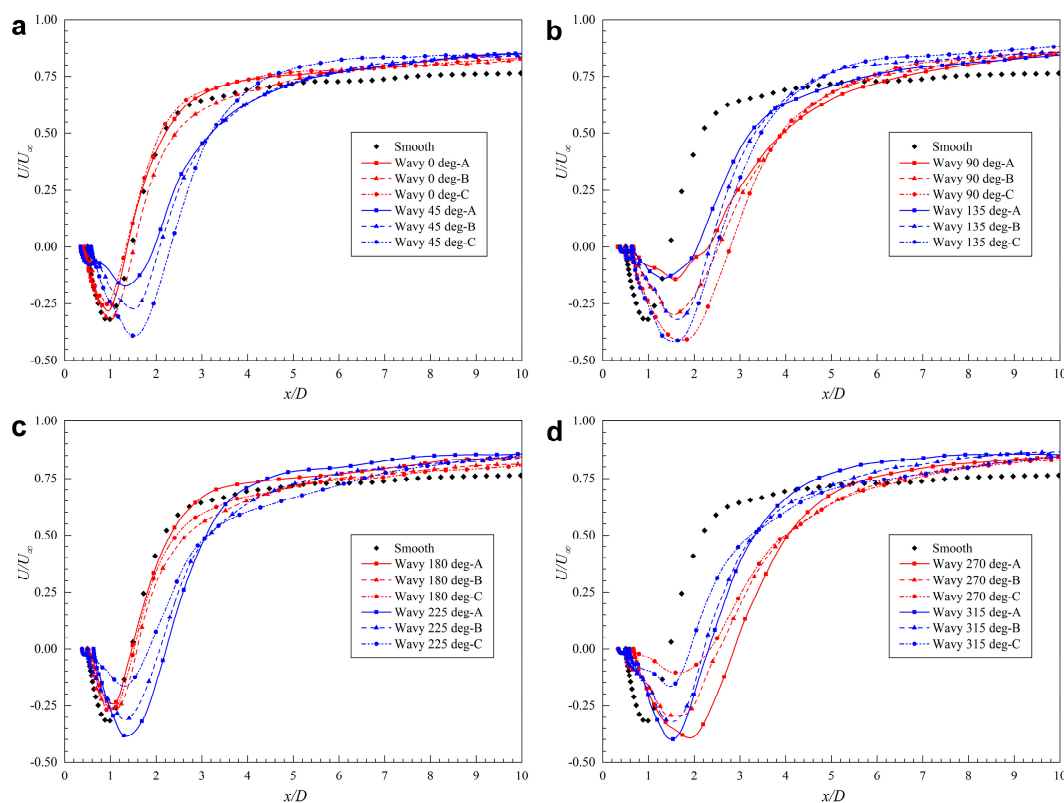


**Figure 6.** Comparison of the average streamwise velocity distributions of the smooth cylinder and wavy cylinder A1 at eight rotation angles. Here, (a)  $\theta = 0^\circ$  and  $45^\circ$ ; (b)  $\theta = 90^\circ$  and  $135^\circ$ ; (c)  $\theta = 180^\circ$  and  $225^\circ$ ; (d)  $\theta = 270^\circ$  and  $315^\circ$ .

Figure 7 shows the normalized r.m.s. value of streamwise velocity fluctuation of the wavy cylinder A1 along the wake center line ( $y = 0$  plane). Similar to Figure 6, the velocities at the three sections along the spanwise direction with eight rotation angles of the cylinder ( $\theta$  from  $0^\circ$  to  $315^\circ$ ) are illustrated. The figure shows that the r.m.s. streamwise velocity of the cylinder has the identical similarity as with the average streamwise velocity, which further verifies the partial similarity of the wavy cylinder in 5.1. Analogously, the maximum velocity positions of  $\theta = 0^\circ$  and  $\theta = 180^\circ$  are almost the same as those of the smooth cylinder, while as to the other angles, the maximum velocity positions are located at the cylinder wake, farther from the cylindrical centerline. Beyond that, the maximum r.m.s values of the streamwise velocity fluctuations of  $\theta = 0^\circ$  and  $\theta = 180^\circ$  are greater than those of the smooth cylinder, while with regard to the other angles, they are substantially smaller, which further indicates that except  $\theta = 0^\circ$  and  $\theta = 180^\circ$ , the other angles can have good control on the wake vortex structures of the cylinder and distinct suppression on the drag and lift fluctuations. These results concluded from Figures 6 and 7 are also consistent with the force coefficients in Table 5 and Figure 5a,b.

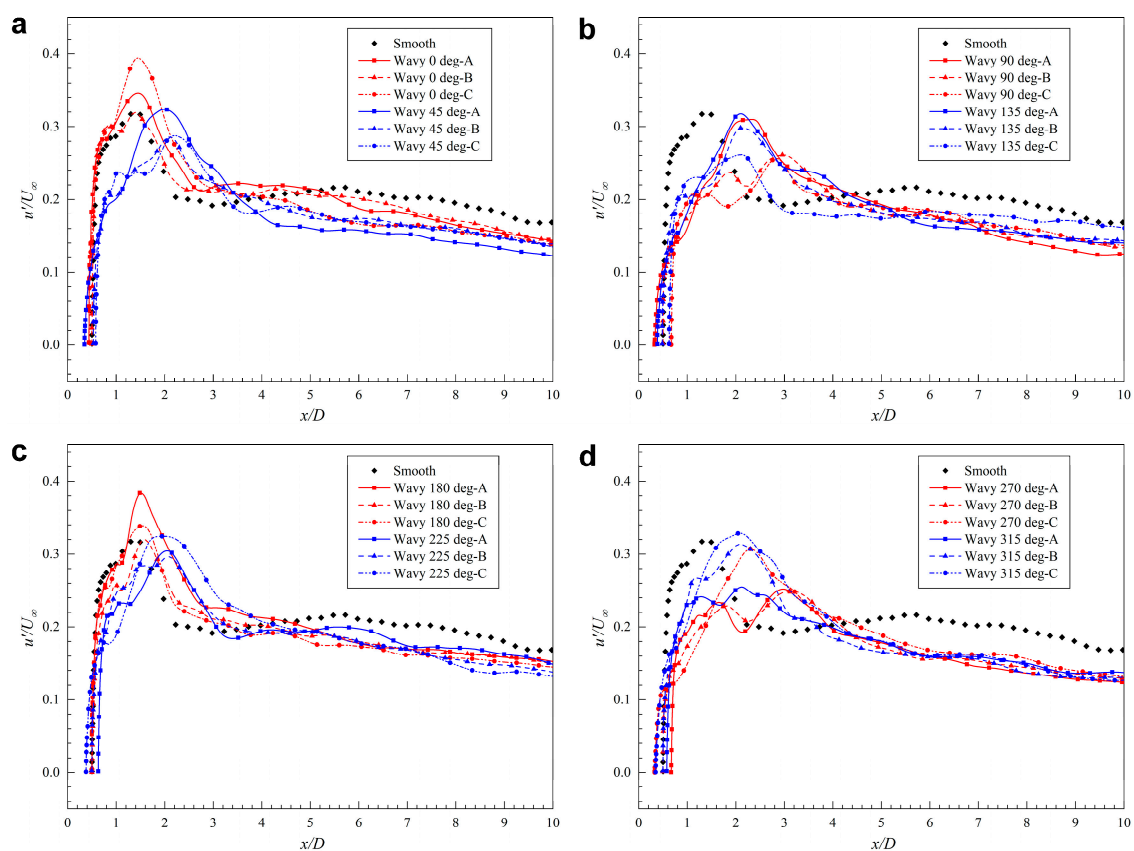


**Figure 7.** Comparison of the r.m.s. streamwise velocity distributions of the smooth cylinder and wavy cylinder A1 at eight rotation angles. Here, (a)  $\theta = 0^\circ$  and  $45^\circ$ ; (b)  $\theta = 90^\circ$  and  $135^\circ$ ; (c)  $\theta = 180^\circ$  and  $225^\circ$ ; (d)  $\theta = 270^\circ$  and  $315^\circ$ .

Due to the partial similarity verification was performed on the wavy cylinder A1, only four rotation angles ( $\theta = 0^\circ, 45^\circ, 90^\circ, 135^\circ$ ) were chosen for wavy cylinders A2 and A3. Figure 8 exhibits the average streamwise velocity and r.m.s. streamwise velocity of the wavy cylinder A2 with  $\alpha = 30^\circ$ . As can be seen from the Figure 8, at  $\theta = 0^\circ$ , the locations of time-averaged closure points and positions of the maximum r.m.s. streamwise velocity are basically the same compared to the smooth cylinder, and the maximum r.m.s. streamwise velocity is greater than that of the smooth cylinder. The zero points and maximum velocity positions of the other three angles are located farther from the centerline in the downstream compared to the smooth cylinder, and the maximum velocity values turn into smaller simultaneously. This result is similar to that obtained from the wavy cylinder A1 with  $\alpha =$

20°. It can be then concluded that except  $\theta = 0^\circ$ , other angles have obvious effects on the control on the wake vortex structures of the cylinder and evident suppression on the drag and lift fluctuations, which agrees well with the force coefficients shown in Figure 5a,b.

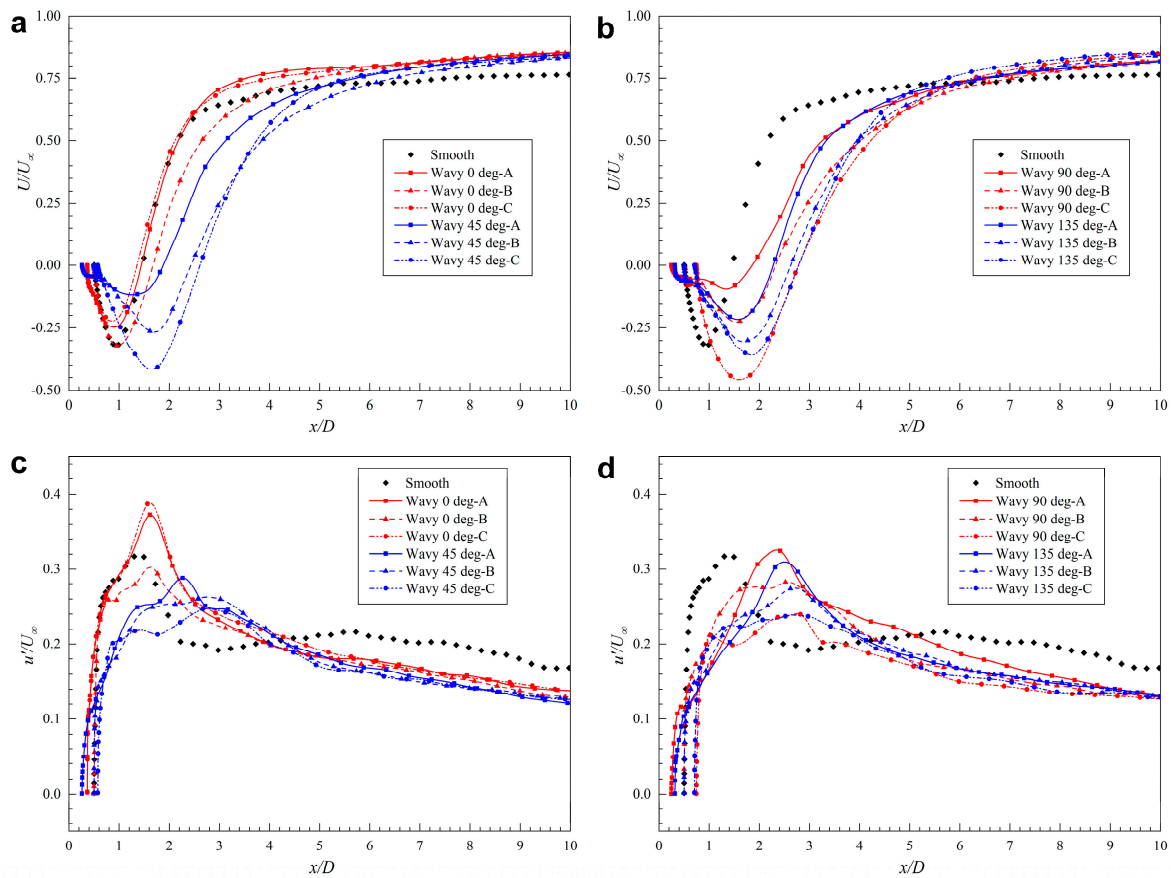


**Figure 8.** Comparison of (a–b) average streamwise velocity and (c–d) r.m.s. streamwise velocity distributions of the smooth cylinder and wavy cylinder A2 at four rotation angles.

Same as the wavy cylinder A2, cylinder A3 also has only four rotation angles ( $\theta = 0^\circ, 45^\circ, 90^\circ, 135^\circ$ ). Figure 9 shows the average streamwise velocity and r.m.s. streamwise velocity of the wavy cylinder A3 with  $\alpha = 40^\circ$ . According to Figure 9, the locations of time-averaged closure points and positions of the maximum r.m.s. streamwise velocity are larger compared to the smooth cylinder. The maximum r.m.s. streamwise velocity is also substantially smaller than that of the smooth cylinder. This is different from the wavy cylinders A1 and A2, cylinder A3 is capable of suppressing the wake vortex structures and the drag and lift fluctuations at four rotation angles. Based on the force coefficients in Figure 5a,b and the force analysis in 5.1, the force coefficients of wavy cylinder A3 decrease much more than that of cylinders A1 and A2 at  $\theta = 0^\circ$ . This is because the zero points and maximum velocity positions are located in the downstream of the wake farther away from the centerline, so that the force coefficients can be well-suppressed. It can also be found that the smaller the maximum r.m.s. streamwise velocity is, the stronger the suppression effect on the drag and lift fluctuations is, indicating better control on the wake vortex structures.

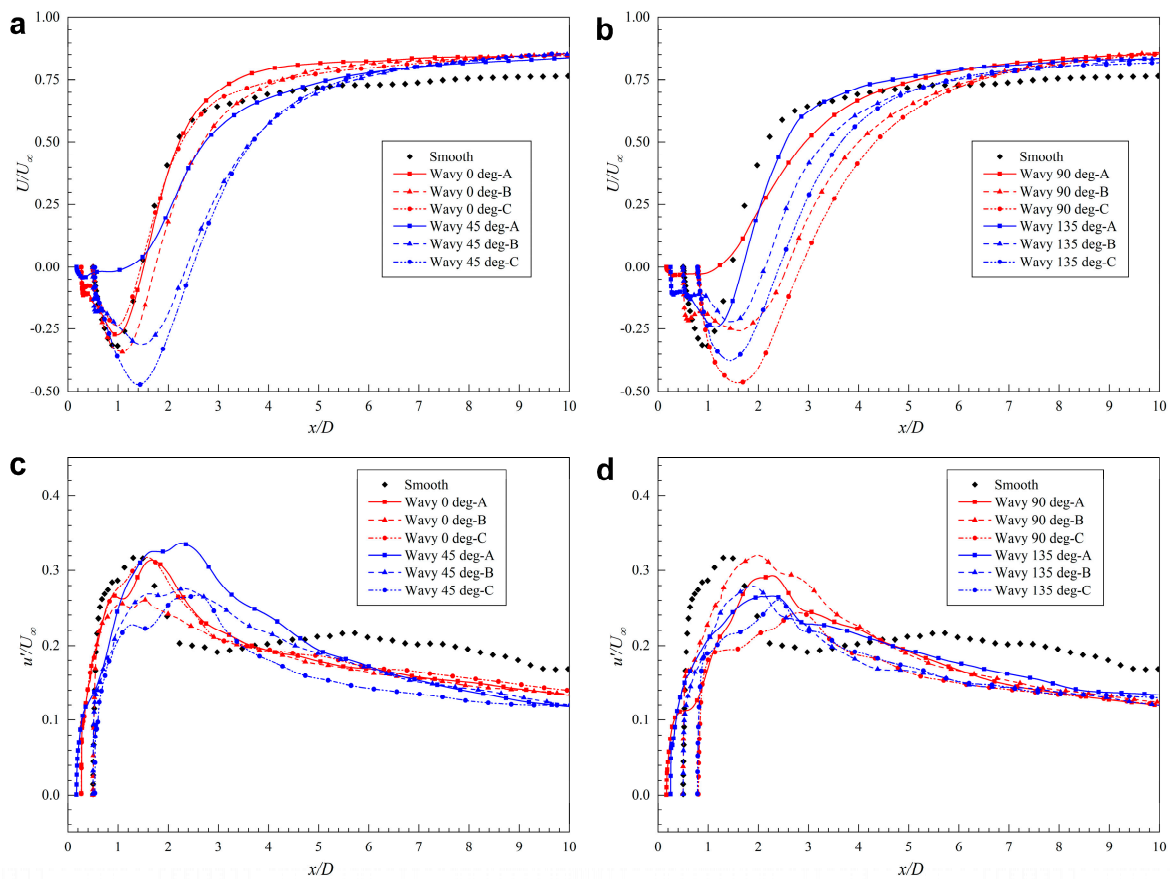


**Figure 9.** Comparison of (a–b) average streamwise velocity and (c–d) r.m.s. streamwise velocity distributions of the smooth cylinder and wavy cylinder A3 at four rotation angles.

Figure 10 shows the wake closure length  $L_{fc}$  and maximum turbulence intensity length  $L_{fu}$  of the three wavy cylinders along the spanwise direction (from Section A to Section C). First, as seen from Figure 10a,b,  $L_{fc}$  and  $L_{fu}$  between  $0^\circ$  to  $135^\circ$  and  $180^\circ$  to  $315^\circ$  are basically the same correspondingly, and the partial similarity of the wavy cylinder is able to be further verified. In addition, when  $\theta = 0^\circ$  and  $\theta = 180^\circ$ , the  $L_{fc}$  of wavy cylinder A1 increases slightly, or even decreases compared to the smooth cylinder, and the maximum increasement in the  $L_{fu}$  is 17%; in terms of other angles, the increasement in the  $L_{fc}$  reaches 28% to 98%, and the  $L_{fu}$  is up to 46% to 128%. Figure 10c,d also depicts that when  $\theta = 0^\circ$ , the  $L_{fc}$  and  $L_{fu}$  of wavy cylinder A2 increase by 16% and 25%, respectively, compared to the smooth cylinder. Compared to cylinder A1, the amplitude slightly increases. At other angles, the increasement in the  $L_{fc}$  reaches 28% to 94% and the  $L_{fu}$  is up to 63%–113%. Thus, the increasement is not significantly varied compared to that of cylinder A1. According to Figure 10e,f, when  $\theta = 0^\circ$ , the  $L_{fc}$  and  $L_{fu}$  of wavy cylinder A3 are increased by a maximum of 22% and 27%, respectively, compared to the smooth cylinder, which are greater than that of the previous two wavy cylinders. At other angles, the maximum increasement in the  $L_{fc}$  is 98% and that in the  $L_{fu}$  is 39%–114%, which is not of much difference from the previous two wavy cylinders.

Based on the analysis of Figure 10,  $L_{fc}$  and  $L_{fu}$  have smaller fluctuation amplitudes at  $\theta = 0^\circ$  ( $180^\circ$ ), and generally increase along the spanwise direction at other angles; as the twisted angle  $\alpha$  of the wavy cylinder increases, fluctuation amplitudes of the  $L_{fc}$  and  $L_{fu}$  also increase gradually. For wavy cylinder A3 with  $\alpha = 40^\circ$ , the minimum value of  $L_{fc}$  is even smaller than that of the smooth cylinder, which may be caused by the increase in the fluctuation range of the wake closure length with the gradually increased curvature of the cylindrical surface. According to the analysis of previous data, when  $\theta = 0^\circ$  ( $180^\circ$ ),  $L_{fc}$  and  $L_{fu}$  gradually increase with the increase of  $\alpha$ ; when  $\theta$  is equal to other angles, the increasement of  $L_{fc}$  and  $L_{fu}$  has minuscule variation with the increase of  $\alpha$ , and are all greater than

that of  $\theta = 0^\circ$  ( $180^\circ$ ). Combined with the force analysis in 5.1, it can be found that when  $\theta = 0^\circ$  ( $180^\circ$ ), the lift and drag reductions of the wavy cylinder increase gradually with the increase of  $\alpha$ . When  $\theta$  is equal to other angles, the lift and drag reductions of different values of  $\alpha$  do not differ much and are greater than that of  $\theta = 0^\circ$  ( $180^\circ$ ). By comparison, it can be concluded that the lift and drag reductions of the wavy cylinders decrease with the increase in the vortex formation lengths  $L_{fc}$  and  $L_{fu}$ . When  $\theta = 0^\circ$  ( $180^\circ$ ), the elongation of vortex formation length is relatively small compared to the smooth cylinder; therefore, the control and suppression effects of the wake vortex structures are also relatively small, leading to the small reductions in the lift and drag. On the contrary, the formation lengths at other angles are greatly elongated, indicating that the wake vortex can be well-controlled and suppressed so that the lift and drag fluctuations can be minimized.

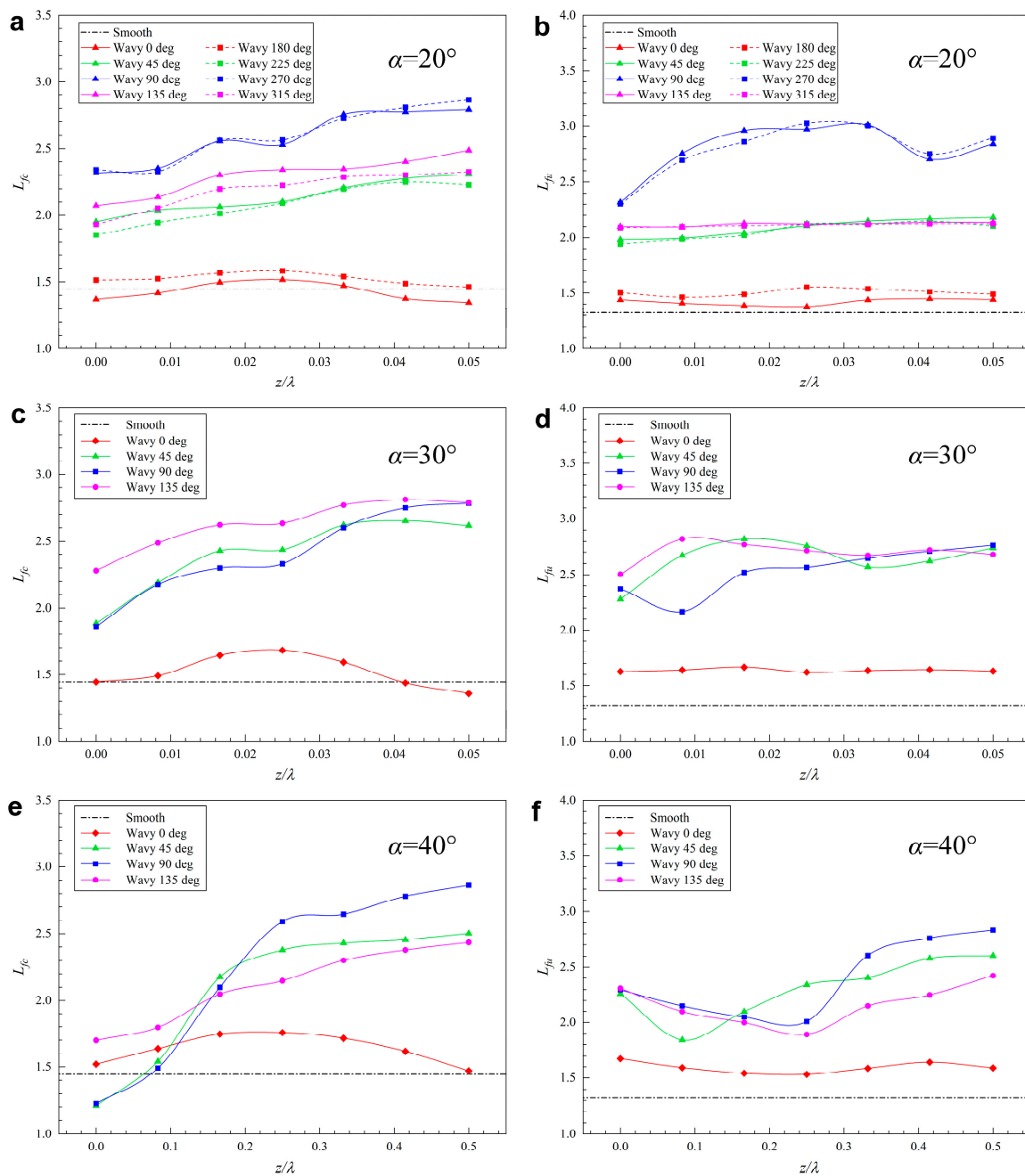


**Figure 10.** Two definitions of the vortex formation length, (a,c,e) the wake closure length ( $L_{fc}$ ) and (b,d,f) the maximum turbulence intensity length ( $L_{fu}$ ), for the smooth cylinder and three wavy cylinders.

### 5.3. Pressure Coefficient and 3D Separation

The drag reductions for different cylinders can be predicted by analyzing the circumferential pressure distributions [30]. Figure 11 shows the average circumferential pressure coefficients of three different sections (A, B, C) for different wavy cylinders, with the smooth cylinder also included for comparison. Figure 11a manifests that with regard to the wavy cylinder A1 with  $\alpha = 20^\circ$ , the pressure coefficient distributions of sections A, B, and C at  $\theta = 0^\circ$  are the same as those of sections C, B, and A at  $\theta = 180^\circ$ , respectively. The same similarities can be found between  $\theta = 45^\circ$  and  $\theta = 225^\circ$ ,  $\theta = 90^\circ$  and  $\theta = 270^\circ$ , and  $\theta = 135^\circ$  and  $\theta = 315^\circ$ , which shows the same regularity as the velocity distributions of cylinder A1 in 5.2. Combining 5.1 and 5.2 can verify that the wavy cylinders have partial similarity. Furthermore, the figure indicates that the positions and values of the minimum pressure coefficient are disparate in different sections. The position of the minimum pressure coefficient of the smooth cylinder is at about  $70^\circ$ , and that of the three sections of cylinder A1 when  $\theta = 0^\circ$  differ little from the smooth cylinder. As  $\theta$  gradually increases, the position of the minimum pressure coefficient of section A increases and section C decreases, while that of section B remains unchanged compared to the smooth cylinder. In addition, when  $\theta = 0^\circ$ , the minimum pressure coefficients of three sections have no obvious difference compared to that of the smooth cylinder; however, as  $\theta$  increases gradually, the minimum pressure coefficients of three sections increase simultaneously, and the maximum value is reached when  $\theta = 90^\circ$ .

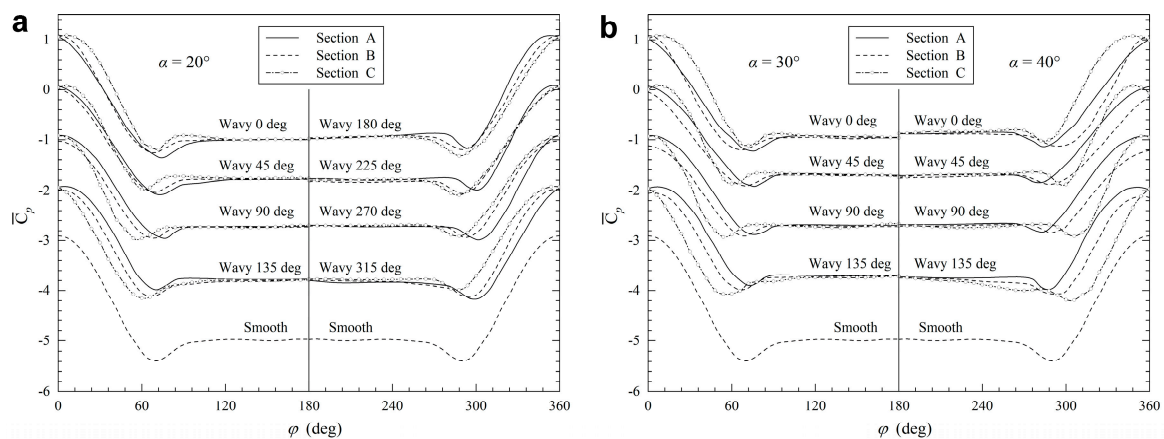


**Figure 11.** Average circumferential pressure coefficient distributions of (a) the wavy cylinder A1 and (b) the wavy cylinders A2 and A3.

Figure 11b shows that the regularities of wavy cylinders A2 and A3 are similar to cylinder A1, and the positions and values of the minimum pressure coefficients at different sections and  $\theta$  are disparate likewise. For cylinder A2, when  $\theta = 0^\circ$ , the positions of the minimum pressure coefficients slightly increase at sections A and C compared to that of the smooth cylinder, while at other rotation angles, they share the same regularity as that of cylinder A1. The minimum pressure coefficients of three sections also slightly increase at  $\theta = 0^\circ$  compared to that of the smooth cylinder, and the values of which increase with the increase of  $\theta$ . The positions and values of the minimum pressure coefficients at four rotation angles of cylinder A3 at sections A and C all have a greater increase than that of the smooth cylinder. The other patterns are basically the same as those of cylinder A2.

As seen in Figure 11, when  $\theta = 0^\circ$ , the positions and values of the minimum pressure coefficients of three wavy cylinders at sections A and C increase with the increase of twisted angle  $\alpha$  compared to that of the smooth cylinder. The variation patterns of three wavy cylinders at other three rotation angles are basically the same. In the subcritical Reynolds number range, the average drag coefficient is directly proportional to  $-\bar{C}_p$  [13], indicating that larger pressure coefficient will result in smaller average drag of the cylinder. This is also consistent with the variation patterns of force coefficients and vortex formation lengths of the wavy cylinders in 5.1 and 5.2.

Figure 11 demonstrates that the positions of the minimum pressure coefficients of the three wavy cylinders at different rotation angles and sections are all different, which means that the separation lines of the cylinders change along the spanwise direction. Figure 12 shows the separation lines along the cylindrical surface of the smooth cylinder and three wavy cylinders at  $\theta = 0^\circ$  and  $90^\circ$ , which are obtained by calculating the streamlines of wall shear stress or the average streamwise velocity. As seen in Figure 12, the wavy cylinders exhibit a three-dimensional separation phenomenon compared to the smooth cylinder. The separation line of the smooth cylinder is a straight line, indicating that the separation points are all at the same position, while the wavy cylinder separation line is wavelike and the positions of the separation points change with the shape of the cylinder. By comparison, the variation amplitude of the separation line shape of the wavy cylinder A1 is smaller and the transition is smoother. The variation amplitude of cylinder A2 is larger than that of A1, and the fluctuation amplitude of the separation line of cylinder A3 reaches the largest with some sharp turning points. It can be found that the three-dimensional wavy separation has a significant influence on the stability of the separated shear layer of the cylindrical turbulent wake vortex and that the influence on the separation line increases with the increase of the cylindrical deformation degree. Therefore, it can be inferred that this strong three-dimensional separation can lead to a more stable development of the cylindrical wake vortex separated shear layer [31,32].

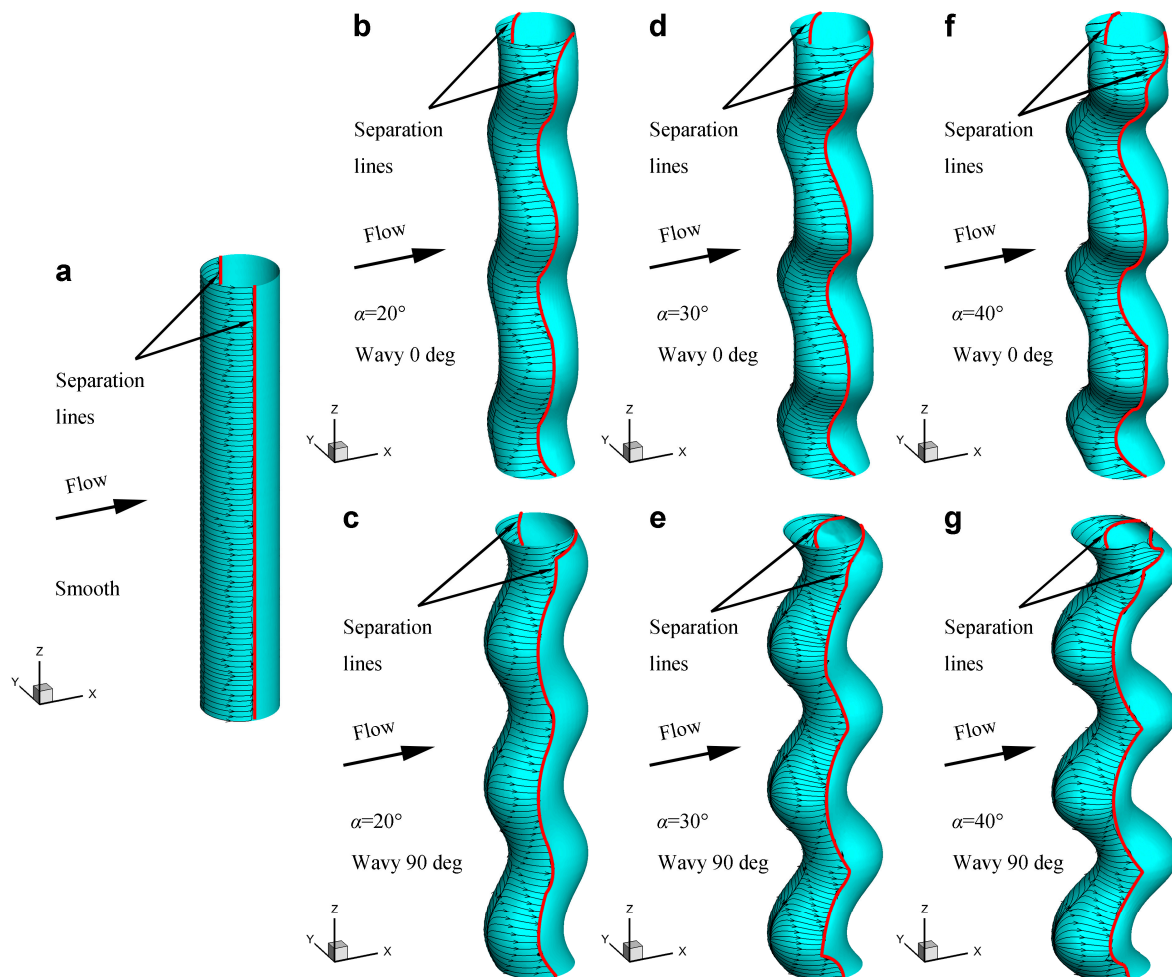


**Figure 12.** Three-dimensional separation lines of (a) the smooth cylindrical surface and (b–g) three wavy cylindrical surfaces.

#### 5.4. Turbulent Kinetic Energy

The turbulent fluctuations around the object are related to the wave force exerted on the object [33]. Figure 13 shows the normalized turbulent kinetic energy  $[TKE = (u'^2 + v'^2 + w'^2)/2U_\infty^2]$  contour plots of different cylindrical wake vortices in the  $x$ - $z$  plane ( $y/D = 0$ ). According to Figure 13a, the smooth cylinder has a very small TKE value from the cylindrical surface to  $x/D = 0.9$  and the maximum TKE interval is located between  $x/D = 1$  and 2.4 in the wake vortex. Along the spanwise direction, the TKE values are evenly distributed. Comparing Figure 13b,d,f, it can be found that when  $\theta = 0^\circ$ , the TKE distribution of the wavy cylinder A1 is basically the same as that of the smooth cylinder. In addition, the smaller TKE value interval of cylinder A2 is slightly shifted downstream and the maximum TKE interval range is slightly decreased, while the TKE distribution along the spanwise direction exhibits a periodic variation and is similar to the geometry of the cylinder. The maximum TKE value at the nodal plane (sections A, C) is greater than that at the saddle plane (section B). The smaller TKE value interval of cylinder A3 is moved further downstream, from the surface of the cylinder to  $x/D = 1.2$ , and the maximum TKE interval range is reduced more than before, located between  $x/D = 1.2$  and 1.8 in the wake vortex. In addition, the periodicity of TKE distribution along the spanwise direction is stronger. The maximum TKE value of the saddle plane (section B) decreases more than that of cylinder A2. The variation of the TKE distribution along the streamwise direction is smaller than the previous cylinders. Comparing Figure 13c,e,g, it can be found that when  $\theta = 90^\circ$ , the smaller TKE value intervals of the three cylinders are basically located from the cylindrical surface to  $x/D = 2$  and the TKE value in this interval largely decreases compared to the smooth cylinder and the three cylinders with  $\theta = 0^\circ$ . The maximum TKE intervals are located between  $x/D = 2.4$  and 2.6 in the wake vortex. Furthermore, due to the obvious decrease in the overall TKE values along the spanwise direction, only a weak periodicity can be observed along the spanwise direction, but the value at the nodal plane (section A) is still larger than that at the saddle plane (section C) and the variations of the overall TKE distribution along the streamwise direction are significantly reduced than before.

According to the analysis of Figure 13, as  $\alpha$  increases, the periodicities of TKE distribution along the spanwise direction of the cylindrical near-wake region and the maximum TKE interval become gradually stronger. The variations in TKE distribution along the streamwise direction, as well as the overall TKE values, decrease gradually compared to the smooth cylinder; especially, when  $\alpha = 40^\circ$ , a huge reduction occurs. The maximum TKE interval range also gradually reduces compared to the smooth cylinder, and the interval position is closer to the downstream of the wake. The overall TKE values at  $\theta = 90^\circ$  is lower than that at  $\theta = 0^\circ$ , which is also consistent with the lift and drag coefficients in 5.1 and the velocity distributions and wake vortex formation lengths in 5.2. The low turbulence intensity of cylinder A3 in Figure 9 corresponds exactly to the low TKE in Figure 13f,g. Therefore, it can be concluded that the significant reduction in the cylindrical wake TKE can result in the reduction in the drag and fluctuating lift of the wavy cylinder.

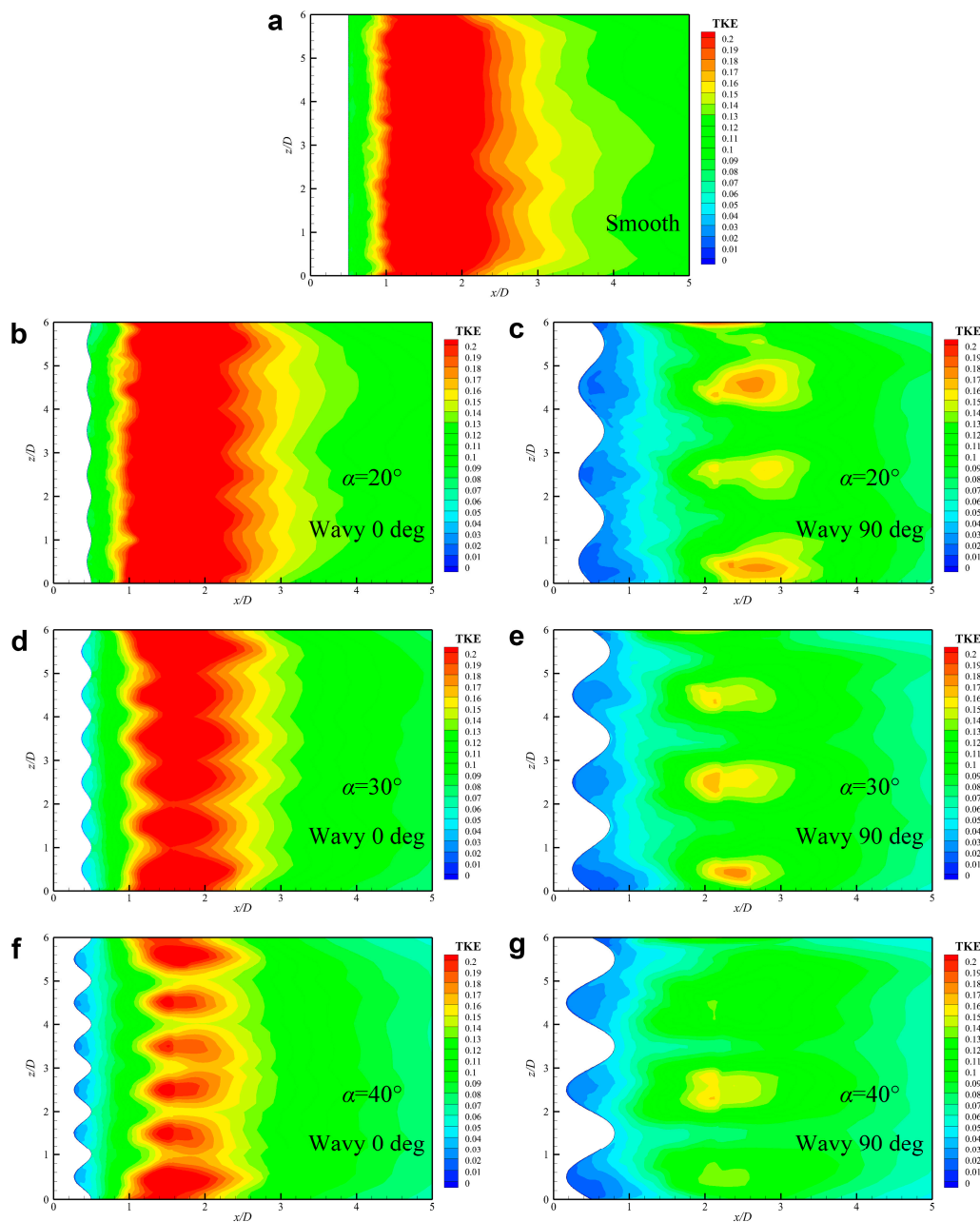


**Figure 13.** Normalized turbulent kinetic energy (TKE) distributions of (a) the smooth cylinder and (b–g) three wavy cylinders in the  $x$ - $z$  plane.

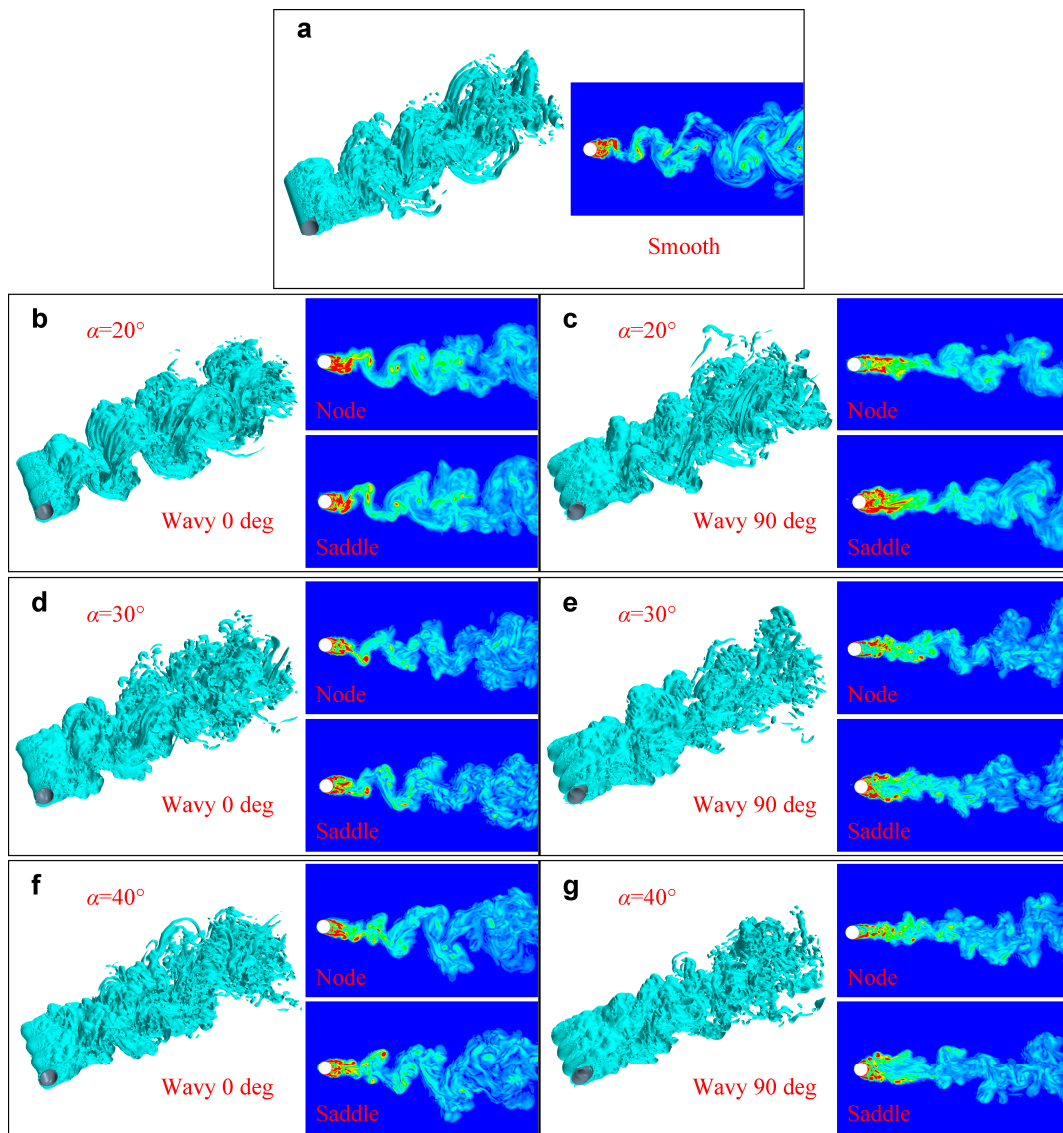
### 5.5. Three-Dimensional Vortex Structures

Figure 14 shows the three-dimensional instantaneous vortices magnitude and the two-dimensional instantaneous vorticity isosurfaces along the spanwise direction at the nodal and saddle planes of different cylinders. The figure depicts a significant discrepancy in free shear layer development and vortex formation length. Figure 14a reveals the isosurfaces of three-dimensional and two-dimensional vortex structures of the smooth cylinder. It can be observed that there exists large-scale Karman vortex street in the cylinder wake region and the oscillation amplitude is large. As can be seen from the two-dimensional vortex structure, the vortex shedding point of the separated shear layer is very close to the cylindrical surface and the vortex magnitude of the near-wake region is large. Figure 14b–g shows that when  $\theta = 0^\circ$ , the vortex distribution of the wake region of cylinder A1 is basically the same as that of the smooth cylinder, and as  $\alpha$  increases, the separation position of the cylindrical wake vortex

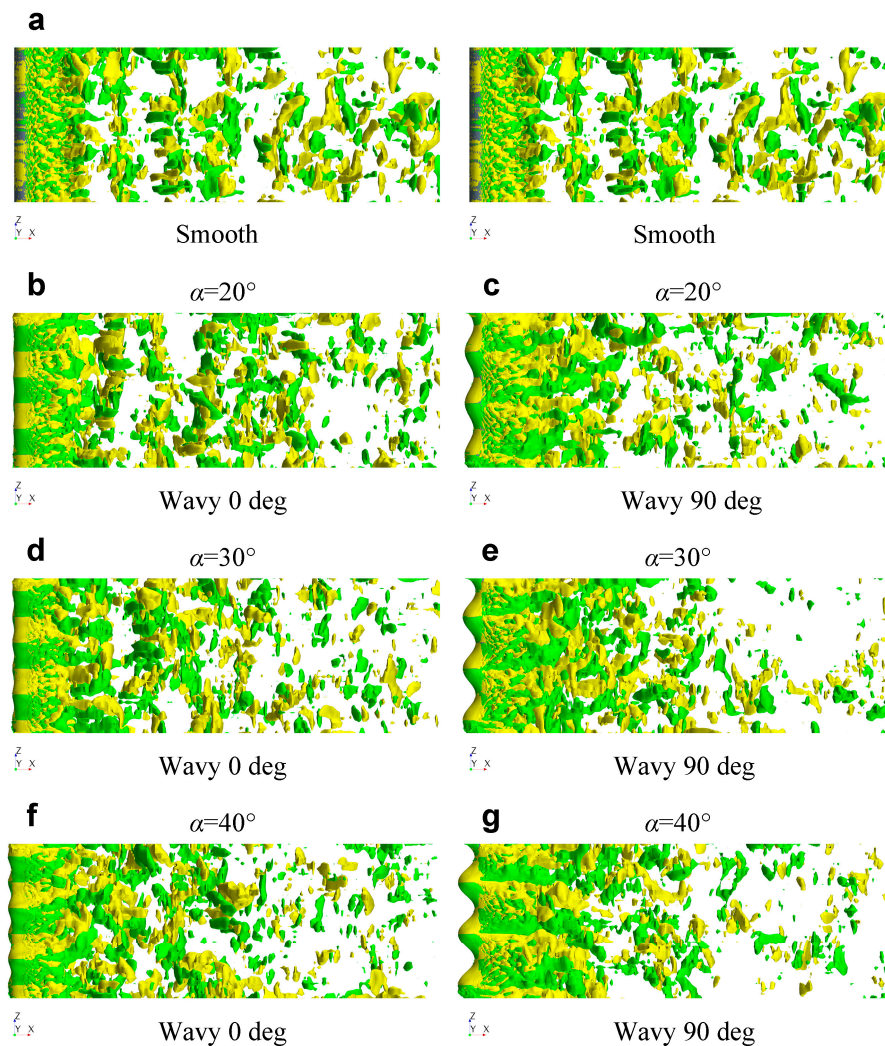
is delayed closer to the downstream. The magnitude of the vortex in the near-wake region is also reduced, and it can be observed that the Karman vortex street reappears in the far wake region, but its fluctuation amplitude is reduced compared to the smooth cylinder. When  $\theta = 90^\circ$ , the three cylindrical shear layers extend longer in the downstream direction and the vortex shedding positions are farther away from the cylindrical surface. The magnitude of the vortex in the near-wake region is significantly reduced compared to before and decreases more with the increase of  $\alpha$ , and this part of the small vortex region becomes larger. A comparison of the nodal and saddle planes shows that because the separation angle is small in the saddle plane, the vortex expands along both streamwise and crosswise directions, resulting in a wider distribution of vortices in the near-wake region. Due to the larger separation angle in the nodal plane, which suppresses the development of the shear layer, the vortex seems to be extended only in the streamwise direction and noticeably suppressed in the crosswise direction. Therefore, the distribution of vortices in the near-wake region becomes narrower, so the vortex structure along the spanwise direction illustrates periodic variations [34]. In addition, as the formation of the initial vortex structure is further delayed in the downstream direction, the strength of Karman vortex street is also weakened in the downstream direction.

Figure 14 suggests that compared to the smooth cylinder, as  $\alpha$  increases, the three cylindrical wake vortex shedding positions and the length of the shear layer along the streamwise direction increase gradually and the small vortex region of the near wake becomes wider. The Karman vortex street reappears at a position further away from the cylindrical surface, but its fluctuation amplitude also reduces gradually. It can also be found that the vortex suppression effect and the elongation length at  $\theta = 90^\circ$  are better than those at  $\theta = 0^\circ$ , which is consistent with the force coefficients in 5.1 and the distributions of TKE in 5.4. The amplitudes of the lift and drag oscillations decrease with a lower intensity of the wake vortex due to the elongation of the cylindrical shear layer and the small vortex region of the near wake.

Figure 15 shows the isosurfaces of the instantaneous crosswise vorticity ( $\omega_y = \pm 15$ ) of different cylinders. According to Figure 15a, the instantaneous crosswise vorticity after the smooth cylinder is very chaotic and the formation length of the vortex in the near-wake region is very small. Figure 15b–g shows that as  $\alpha$  increases, the shedding length of the cylindrical wake vortex increases. Especially, the shedding length of the vortex at  $\theta = 90^\circ$  is much larger than that at  $\theta = 0^\circ$ . The development of crosswise vortices in the near-wake region also becomes more coherent and well-organized, which also means that the three-dimensional free shear layer of the cylindrical surface is more difficult to develop and is transformed into mature vortex structure in the downstream far away from the cylinder. Compared to the force coefficients in 5.1 and the velocity distributions in 5.2, it can also be found that the wake vortex shedding position is further away from the cylindrical surface, meaning that longer vortex formation length will result in greater drag and lift reductions.



**Figure 14.** Comparison of the instantaneous three-dimensional vortices magnitude and spanwise two-dimensional vorticity isosurfaces of the smooth cylinder and three wavy cylinders. Here, (a) smooth cylinder; (b)  $\alpha = 20^\circ$  and  $\theta = 0^\circ$ ; (c)  $\alpha = 20^\circ$  and  $\theta = 90^\circ$ ; (d)  $\alpha = 30^\circ$  and  $\theta = 0^\circ$ ; (e)  $\alpha = 30^\circ$  and  $\theta = 90^\circ$ ; (f)  $\alpha = 40^\circ$  and  $\theta = 0^\circ$ ; (g)  $\alpha = 40^\circ$  and  $\theta = 90^\circ$ .



**Figure 15.** Comparison of the crosswise vorticity isosurfaces ( $\omega_y = \pm 15$ ) of the smooth cylinder and three wavy cylinders. Here, (a) smooth cylinder; (b)  $\alpha = 20^\circ$  and  $\theta = 0^\circ$ ; (c)  $\alpha = 20^\circ$  and  $\theta = 90^\circ$ ; (d)  $\alpha = 30^\circ$  and  $\theta = 0^\circ$ ; (e)  $\alpha = 30^\circ$  and  $\theta = 90^\circ$ ; (f)  $\alpha = 40^\circ$  and  $\theta = 0^\circ$ ; (g)  $\alpha = 40^\circ$  and  $\theta = 90^\circ$ .

## 6. Conclusions and Prospect

Vortex-induced vibration occurs on marine platforms and risers under the action of ocean currents and has a significant effect on the fatigue damage and safety problems. It is necessary to accurately predict the response of the vibrations under various inflow conditions, so as to adopt effective measures to restrain the damage of the vortex-induced vibrations to the marine platforms and risers. This paper traces the latest research trends of vortex-induced vibrations on cylinders. This study simulates the turbulent flow of wavy cylinders with a Reynolds number of 28712 by using large eddy simulation based on the finite volume method. For comparison, the calculations were performed on a smooth cylinder as well. By analyzing the variations in the velocity distributions and the vortex formation lengths, the positions and values of the minimum circumferential pressure coefficients, the shape changes of the separation line, and the overall TKE distributions of the cylinder wake, it was concluded that the optimized wavy cylinder has better control on the wake vortex structure and more stable development of the free shear layer, and can lead to greater drag reduction and better suppression of lift fluctuations.

Marine risers and submarine pipelines are indispensable equipment for deep-water oil and gas exploitation. Under the action of ocean currents, risers and pipelines will produce strong vortex-induced vibrations, which is an important factor for fatigue damage of structures. By employing this kind of

wavy cylinder, the forces and vortex-induced vibrations suffered from currents can be greatly reduced without changing the cross-section shape and diameter of the cylinder, which can ensure the working performance of offshore platforms and prolong the fatigue life of risers and pipelines. However, there exist difficulties and costs in designing and manufacturing due to its special construction while adopting the wavy cylinder into practice. Several problems including fatigue and structural strength as well as vibration characteristics need to be further investigated before this wavy cylinder can be utilized in practice.

**Author Contributions:** Conceptualization and Methodology: C.G. and K.S.; simulation and investigation: H.G. and J.H.; analysis and validation: C.G. and H.G.; writing—original draft: H.G. and W.Z.; writing—review and editing: J.H. and K.S.; revision and supervision: W.Z. and W.W.

**Funding:** This research was funded by the National Natural Science Foundation of China, grant number 51679045 and 51579052.

**Acknowledgments:** This research was supported in part with computational resources at the Harbin Engineering University. This research thanks Tiecheng Wu and Jie Gong, and so on, for their help and guidance. The authors would like to thank the anonymous reviewers and the editors for their comments.

**Conflicts of Interest:** The authors declare no conflict of interest.

## References

1. Placzek, A.; Sigrist, J.F.; Hamdouni, A. Numerical simulation of an oscillating cylinder in a cross-flow at low Reynolds number: Forced and free oscillations. *Comput. Fluids* **2009**, *38*, 80–100. [[CrossRef](#)]
2. Pastò, S. Vortex-induced vibrations of a circular cylinder in laminar and turbulent flows. *J. Fluids Struct.* **2008**, *24*, 977–993. [[CrossRef](#)]
3. Zhao, M.; Cheng, L. Vortex-induced vibration of a circular cylinder of finite length. *Phys. Fluids* **2014**, *26*, 015111. [[CrossRef](#)]
4. Wang, R.; Xin, D.; Ou, J. Experimental investigation on suppressing circular cylinder VIV by a flow control method based on passive vortex generators. *J. Wind Eng. Ind. Aerodyn.* **2019**, *187*, 36–47. [[CrossRef](#)]
5. Zhu, H.; Yao, J.; Ma, Y.; Zhao, H.; Tang, Y. Simultaneous CFD evaluation of VIV suppression using smaller control cylinders. *J. Fluids Struct.* **2015**, *57*, 66–80. [[CrossRef](#)]
6. Kang, Z.; Zhang, C.; Ma, G.; Ni, W. A numerical investigation of two-degree-of-freedom VIV of a circular cylinder using the modified turbulence model. *Ocean Eng.* **2018**, *155*, 211–226. [[CrossRef](#)]
7. Belloli, M.; Giappino, S.; Morganti, S.; Muggiasca, S.; Zasso, A. Vortex induced vibrations at high Reynolds numbers on circular cylinders. *Ocean Eng.* **2015**, *94*, 140–154. [[CrossRef](#)]
8. Zou, L.; Lin, Y. Force reduction of flow around a sinusoidal wavy cylinder. *J. Hydrodyn.* **2009**, *21*, 308–315. [[CrossRef](#)]
9. Zhuang, Y.Q.; Sun, X.J.; Huang, D.G. Numerical study of unsteady flows past a rotating wavy cylinder. *Eur. J. Mech. B Fluids* **2018**, *72*, 538–544. [[CrossRef](#)]
10. Xu, C.Y.; Ni, Z.Q. Novel characteristics of wavy cylinder in supersonic turbulent flow. *Eur. J. Mech. B Fluids* **2018**, *67*, 158–167. [[CrossRef](#)]
11. Lam, K.; Wang, F.H.; So, R.M.C. Three-dimensional nature of vortices in the near wake of a wavy cylinder. *J. Fluids Struct.* **2004**, *19*, 815–833. [[CrossRef](#)]
12. Lam, K.; Lin, Y.F. Large eddy simulation of flow around wavy cylinders at a subcritical Reynolds number. *Int. J. Heat Fluid Flow* **2008**, *29*, 1071–1088. [[CrossRef](#)]
13. Jung, J.H.; Yoon, H.S. Large eddy simulation of flow over a twisted cylinder at a subcritical Reynolds number. *J. Fluid Mech.* **2014**, *759*, 579–611. [[CrossRef](#)]
14. Zhou, B.; Wang, X.; Guo, W.; Gho, W.M.; Tan, S.K. Experimental study on flow past a circular cylinder with rough surface. *Ocean Eng.* **2015**, *109*, 7–13. [[CrossRef](#)]
15. Wong, K.W.L.; Zhao, J.; LoJacono, D.; Thompson, M.C.; Sheridan, J. Experimental investigation of flow-induced vibration of a rotating circular cylinder. *J. Fluid Mech.* **2017**, *829*, 486–511. [[CrossRef](#)]
16. Jie, H.; Liu, Y.Z. Large eddy simulation and proper orthogonality decomposition of turbulent flow around a vibrissa-shaped cylinder. *Int. J. Heat Fluid Flow* **2017**, *67*, 261–277. [[CrossRef](#)]

17. Yeon, S.M.; Yang, J.; Stern, F. Large-eddy simulation of the flow past a circular cylinder at sub- to super-critical Reynolds numbers. *Appl. Ocean Res.* **2016**, *59*, 663–675. [[CrossRef](#)]
18. Deardorff, J.W. The use of subgrid transport equations in a three-dimensional model of atmospheric turbulence. *J. Fluids Eng.* **1973**, *95*, 429. [[CrossRef](#)]
19. Nicoud, F.; Ducros, F. Subgrid-scale stress modelling based on the square of the velocity gradient tensor. *Flow Turbul. Combust.* **1999**, *62*, 183–200. [[CrossRef](#)]
20. Deardorff, J.W. A numerical study of three-dimensional turbulent channel flow at large Reynolds numbers. *J. Fluid Mech.* **1970**, *41*, 453–480. [[CrossRef](#)]
21. CD-Adapco, S. *STAR CCM+ User Guide Version 12.04*; CD-Adapco: New York, NY, USA, 2017.
22. Leonard, B.P. The ultimate conservative difference scheme applied to unsteady one-dimensional advection. *Comput. Methods Appl. Mech. Eng.* **1991**, *88*, 17–74. [[CrossRef](#)]
23. Baek, D.G.; Yoon, H.S.; Jung, J.H.; Kim, K.S.; Paik, B.G. Effects of the advance ratio on the evolution of a propeller wake. *Comput. Fluids* **2015**, *118*, 32–43. [[CrossRef](#)]
24. Sumer, B.M.; Fredsøe, J. *Hydrodynamics Around Cylindrical Structures*; World Scientific Publishing: Singapore, 1997.
25. Bloor, S. The transition to turbulence in the wake of a circular cylinder. *J. Fluid Mech.* **1966**, *19*, 290–304. [[CrossRef](#)]
26. Gerrard, J.H. The wakes of cylindrical bluff bodies at low Reynolds number. *Philos. Trans. R. Soc. Lond. Ser. A Math. Phys. Eng. Sci.* **1978**, *288*, 351–382. [[CrossRef](#)]
27. Woo, H.G.C.; Cermak, J.E.; Peterka, J.A. On vortex locking-on phenomenon for a cable in linear shear-flow. *J. Wind Eng. Ind. Aerodyn.* **1983**, *14*, 289–300. [[CrossRef](#)]
28. Norberg, C. LDV-measurements in the near wake of a circular cylinder. In *Proceedings of the 1998 ASME Fluids Engineering Division Summer Meeting*; American Society of Mechanical Engineers: Washington, DC, USA, 1998; FED-Volume 245, FEDSM98-5202.
29. Govardhan, R.; Williamson, C.H.K. Mean and fluctuating velocity fields in the wake of a freely-vibrating cylinder. *J. Fluids Struct.* **2001**, *15*, 489–501. [[CrossRef](#)]
30. Bearman, P.W. Investigation of the flow behind a two-dimensional model with a blunt trailing edge and fitted with splitter plates. *J. Fluid Mech.* **1965**, *21*, 241–255. [[CrossRef](#)]
31. Zhang, W.; Dai, C.; Lee, S.J. PIV measurements of the near-wake behind a sinusoidal cylinder. *Exp. Fluids* **2005**, *38*, 824–832. [[CrossRef](#)]
32. Xu, C.Y.; Chen, L.-W.; Lu, X.Y. Large-eddy simulation of the compressible flow past a wavy cylinder. *J. Fluid Mech.* **2010**, *665*, 238–273. [[CrossRef](#)]
33. Wu, J.-Z.; Lu, X.-Y.; Zhuang, L.-X. Integral force acting on a body due to local flow structures. *J. Fluid Mech.* **2007**, *576*, 265–286. [[CrossRef](#)]
34. Chyu, C.K.; Rockwell, D. Near-wake flow structure of a cylinder with a helical surface perturbation. *J. Fluids Struct.* **2002**, *16*, 263–269. [[CrossRef](#)]

